Memoirs of the Faculty of Science, Kyoto University, Series of Physics, Astrophysics, Geophysics and Chemistry, Vol. XXXXI, No. 1, Article 2, 2000

Study of Parity Nonconserving Spin Rotation in Neutron-Nucleus Resonance

By

Tomohito Haseyama

Department of Physics, Faculty of Science, Kyoto University
Kyoto 606-8502, Japan

(Received December 20, 1999)

Abstract

We measured the parity nonconserving spin rotation of neutrons transmitted through a ^{139}La target in the 0.74-eV p-wave resonance, in order to determine the weak matrix element in the hadronic interaction. The rotation angle was obtained by the neutron transmission through a target of 5 cm long placed in between two sets of polarized ^{3}He spin filters whose polarization vectors were transverse to the neutron beam and orthogonal to each other. We obtained the peak-to-peak value of the spin rotation as $(7.44 \pm 1.09) \times 10^{-3}$ rad/cm. It is consistent with previous experiments, but experimental accuracy is largely improved. Applying the s-p mixing model, we obtained the weak matrix element as $xW = (1.71 \pm 0.25)$ meV. The value is consistent with the ones deduced from the longitudinal asymmetry in the same resonance.

Contents

1 Introduction 135
1.1 Symmetry on Space Inversion 135
1.2 Large Enhancement of Parity Nonconserving Effects 135
1.3 Overview of the Past Experiments 139
1.4 Present Work for the Measurement of the Parity-Nonconserving Neutron-Spin Rotation 140

2 Experimental Procedure 141
2.1 Accelerator Complex and Spallation Neutron Source 141

2.2 Neutron Flux Monitor 144
2.3 Neutron Spin Polarizer 146
2.4 Upstream Spin Transport Magnet 147
2.5 Lanthanum Target and Superconducting Magnetic Shield 148
2.6 Downstream Spin Transport Magnet 150
2.7 Neutron Spin Analyzer 150
2.8 Neutron Absorber Foils 151
2.9 Neutron Transmission Detector 151
2.10 Data Taking 153

3 Analysis **154**
3.1 Analysis Formulae 154
3.1.1 Transmission of Neutrons through Polarized ^3He Nuclei . . . 154
3.1.2 Asymmetry due to Spin Rotation Angle and Residual Magnetic Field 156
3.2 Data Analysis 156
3.2.1 Determination of Kinetic Energies of Neutrons in Beam 156
3.2.2 Analysis of NMR Signals 158
3.2.3 Background Estimation in Neutron Transmission 160
3.2.4 Neutron Transmission Enhancement and its Relation to NMR 162
3.2.5 Determination of the Shape of the P-wave Resonance of ^{139}La 164
3.2.6 Extraction of Spin Rotation Angle 166

4 Results and Discussion **170**

5 Conclusion **173**

A Optical Pumping **174**

B Principle of Adiabatic Fast Passage NMR **175**

Chapter 1

Introduction

1.1 Symmetry on Space Inversion

Parity, a quantum number related to a discrete symmetry of space inversion, has been playing an important role in particle and nuclear physics. If the physical laws remain unchanged under the space inversion, parity is conserved. Until 1956 the physical laws describing all the four fundamental interactions had been thought to be unchanged in space inversion. However, an experimental evidence of parity nonconservation was found in β-decay of ^{60}Co by Wu et al. in 1957 [1]. They observed asymmetric emission of electrons with respect to the direction of the polarization of mother nuclei. After the discovery, many experimental studies on leptonic and semi-leptonic processes revealed the mechanism of the weak interaction and the origin of parity nonconservation. Although the weak interaction is caused by exchanges of the gauge bosons, $W^{\pm}$ and Z^0, in the Weinberg-Salam model, we still have little knowledge of the weak interaction in hadronic reactions, where the strong interaction among quarks is so strong that the effect of the weak interaction appears small and is easily smeared out.

1.2 Large Enhancement of Parity Nonconserving Effects

The masses of the weak bosons are so heavy that the Compton wave-lengths of the weak bosons are much shorter than a typical distance between nucleons in the nucleus. Thus direct exchanges of the weak bosons between nucleons are greatly suppressed. The parity nonconserving interaction between two nucleons originates mainly from exchanges of π, ρ, or ω, where one of the vertices is a coupling of the strong interaction and the other is of the weak interaction. The order of the relative strength of the weak interaction to the strong interaction can be approximately estimated as $G_F m_\pi^2/4\pi \sim 2 \times 10^{-7}$, where G_F and m_π are the Fermi coupling constant and the mass of pion, respectively. The experimental results on the parity nonconserving longitudinal asymmetry in proton-proton scattering, $A_L(pp)$, are listed in Table 1.1. The experimental results can be explained with the interference between

incident energy (MeV)	$A_L(pp)$	reference
15	$(-1.7 \pm 0.8) \times 10^{-7}$	[2]
15	$(-2.3 \pm 0.8) \times 10^{-7}$	[3]
45	$(-1.3 \pm 0.8) \times 10^{-7}$	[4]
221	$(+0.34 \pm 0.67) \times 10^{-7}$	[5]
800	$(+2.4 \pm 1.1 \pm 0.1) \times 10^{-7}$	[6]

Table 1.1: Experimental results of the longitudinal asymmetries in proton-proton scattering.

$^1S_0$ and $^3P_0$ amplitudes and the interference between $^3P_2$ and $^1D_2$ amplitudes.

It was discovered that effects of parity nonconservation are strongly amplified in many p-wave resonances in the interactions of polarized neutron and unpolarized nucleus. Such an amplification is of great interest in studying the weak interaction in hadronic reactions.

In particular, a helicity asymmetry of about 10% was observed for neutron transmission in the p-wave resonance of ^{139}La around 0.74 eV, which corresponded to the enhancement of about 10^6 in comparison with the asymmetries in proton-proton scattering. Such enhancements have been seen in many p-wave resonances in neutron nucleus reactions. As a theoretical explanation for such a large longitudinal asymmetries, a model considering the interference between p-wave and its neighboring s-wave resonances was proposed. The model is called the "s-p mixing model". According to the s-p mixing model, a large enhancement can happen when an s-wave resonance and a p-wave resonance exist close to each other. The parity nonconserving effect appears in several measurable quantities in addition to the longitudinal asymmetry of the total cross section. One of them is the rotation of neutron spin around the momentum direction while being transmitted through material.

According to the s-p mixing model, for neutrons whose energy E_n is in the vicinity of the energy of a p-wave resonance, the neutron spin rotation angle in unit length, $\frac{\partial\phi}{\partial z}$, is expected as

$$\frac{\partial\phi}{\partial z} \simeq \frac{4\pi g N}{k_n^2} \frac{xW(\Gamma_s^n \Gamma_p^n)^{\frac{1}{2}}}{E_p - E_s} \frac{E_n - E_p}{(E_n - E_p)^2 + \frac{1}{4}\Gamma_p^2}, \tag{1.1}$$

whereas the difference of the cross sections for different helicities of the incident neutrons, $\Delta\sigma$, is expected as

$$\Delta\sigma \simeq \frac{4\pi g}{k_n^2} \frac{xW(\Gamma_s^n \Gamma_p^n)^{\frac{1}{2}}}{E_p - E_s} \frac{\Gamma_p}{(E_n - E_p)^2 + \frac{1}{4}\Gamma_p^2} , \tag{1.2}$$

where W is the weak matrix element for the transition between the s-wave and the p-wave resonances, N is the number density of the target nuclei, E_n and k_n are the neutron energy and the wave number, respectively. And E_s, Γ_s, and Γ_s^n are the energy, the total width, and the neutron width of the s-wave resonance, respectively. Likewise, E_p, Γ_p, and Γ_p^n are those of the p-wave resonance. The spin statistical factor g is calculated with the spin of the target nucleus, I, and that of the resonance state, J, as

$$g = \frac{2J+1}{2(2I+1)} . \tag{1.3}$$

The x is defined as

$$x^2 = \frac{\Gamma_{p_{1/2}}^n}{\Gamma_p^n} , \tag{1.4}$$

where $\Gamma_{p_{1/2}}^n$ is the partial neutron width for the p-wave neutrons whose orbital and spin angular momenta make a total angular momentum of $j = 1/2$. It is clear from Equations (1.1) and (1.2) that the parity nonconserving effects become large when the s-wave and the p-wave resonances are close in energy to each other.

Here we describe how the effects of the parity nonconservation appear in Equations (1.1) and (1.2) in the framework of the s-p mixing model.

According to the optical theorem, an interaction between a low energy neutron and a nucleus is described with $f(0)$, a forward scattering amplitude. The $f(0)$ has a relation with the total cross section σ as

$$\sigma = \frac{4\pi}{k_n} Imf(0) , \tag{1.5}$$

where k_n is a wave number of incident neutron. It has also a relation with the phase shift in the target δ as

$$\frac{\delta}{Nl} = -\frac{2\pi}{k_n} Ref(0) , \tag{1.6}$$

where l is the target length. Considering only s-wave and p-wave components, $f(0)$ is expressed as

$$f(0) = F_0 + F_1 \boldsymbol{\sigma_n} \cdot \boldsymbol{I} + F_2 \boldsymbol{\sigma_n} \cdot (\hat{\boldsymbol{k}}_n \times \boldsymbol{I}) + F_3 \boldsymbol{\sigma_n} \cdot \hat{\boldsymbol{k}}_n + F_4 \boldsymbol{I} \cdot \hat{\boldsymbol{k}}_n , \tag{1.7}$$

where $\boldsymbol{\sigma_n}$ is an operator for the spin direction of neutron, $\boldsymbol{I}$ is the spin direction of nucleus, $\hat{\boldsymbol{k}}_n$ is the neutron-momentum direction, and $F_i (i = 0 \sim 4)$ are the coefficients as functions of neutron energy. The terms, $\boldsymbol{\sigma_n} \cdot (\boldsymbol{I} \times \hat{\boldsymbol{k}}_n)$, $\boldsymbol{\sigma_n} \cdot \hat{\boldsymbol{k}}_n$, and $\boldsymbol{I} \cdot \hat{\boldsymbol{k}}_n$ are parity nonconserving amplitudes.

In the case of unpolarized target, the terms with F_1, F_2 and F_4 vanish, and the

forward scattering amplitude is simply described as

$$f(0) = F_0 + F_3 \boldsymbol{\sigma_n} \cdot \hat{\boldsymbol{k}}_{\boldsymbol{n}} \ . \tag{1.8}$$

Thus the spin rotation angle around the momentum direction and the difference of the cross sections for the different neutron helicities are given, respectively, as

$$\frac{\partial \phi}{\partial z} = -\frac{4\pi}{k_n} N Re F_3 \, , \tag{1.9}$$

and

$$\Delta\sigma = \frac{8\pi}{k_n} Im F_3 \, . \tag{1.10}$$

According to the s-p mixing model, the parity nonconserving amplitude F_3 is caused by the interference between a p-wave resonance and neighboring s-wave resonances. Now we assume that only one s-wave and one p-wave resonances contribute to the interference. Due to the interference between the s-wave and the p-wave resonances with the matrix element W, it becomes possible that a neutron is captured by the nucleus as s-wave (p-wave) and then emitted from the nucleus as p-wave (s-wave). The sum of the above two processes are regarded to contribute to the parity nonconserving amplitude, F_3. Although the total angular momentum j of the p-wave neutron is either 1/2 or 3/2, only the component of $j = 1/2$ contributes to the interference because of the conservation of the total angular momentum. Thus the exact form of F_3 is given as

$$F_3 = -\frac{g}{k_n} \frac{x W (\Gamma_s^n \Gamma_p^n)^{\frac{1}{2}}}{(E_n - E_s + \frac{i}{2}\Gamma_s)(E_n - E_p + \frac{i}{2}\Gamma_p)} \ . \tag{1.11}$$

Here we assume

$$\Gamma_s << |E_p - E_s| \ , \tag{1.12}$$

and

$$|E_n - E_p| << |E_p - E_s| \ . \tag{1.13}$$

Then the parity nonconserving amplitude is approximated as

$$F_3 \simeq -\frac{g}{k_n} \frac{x W (\Gamma_s^n \Gamma_p^n)^{\frac{1}{2}}}{(E_p - E_s)(E_n - E_p + \frac{i}{2}\Gamma_p)} \ . \tag{1.14}$$

Combining Equations (1.9),(1.10), and (1.14), the neutron spin rotation and the difference of the cross sections for different helicities are obtained as Equations (1.1) and (1.2).

As shown in Equation (1.14), the parity nonconserving amplitude is determined as the product of x and W. Accordingly, the longitudinal asymmetry of the cross section and the neutron spin rotation angle are tightly related to each other. Thus independent determinations of the value xW by the measurement of the spin rotation angle and that of the longitudinal asymmetry provide crucial tests of the enhancement mechanism.

1.3 Overview of the Past Experiments

The first observation of the neutron spin rotation was performed in 1980 at Institut Laue Langevin by Forte et al. [7]. In this experiment, they measured the spin rotation through a ^{117}Sn target using cold neutron beams of about 1.7 meV. They obtained the rotation angle of $(+36.7 \pm 2.7) \times 10^{-6}$ rad/cm. This work was immediately followed by other experiment measuring the longitudinal asymmetry by Kolomensky et al.[8]. They measured the longitudinal asymmetries for ^{117}Sn and ^{139}La targets at neutron energies of about 25 meV. They obtained the longitudinal asymmetries with respect to the total cross sections as $(+6.2 \pm 0.7) \times 10^{-6}$ for ^{117}Sn and $(+9.0 \pm 1.4) \times 10^{-6}$ for ^{139}La. The reactions in these experiments occurred mainly with s-wave neutrons, since the energies were quite low. Admixtures of tails of p-wave resonances were considered to be the source of parity violation.

The first measurement of parity nonconservation which covered p-wave resonances was performed by Alfimenkov et al. in 1982 [9]. They measured the longitudinal asymmetry of the total cross section in the 1.3-eV p-wave resonance of ^{117}Sn. They obtained the longitudinal asymmetry with respect to the p-wave cross section as $(+4.5 \pm 1.3) \times 10^{-3}$. Precise measurements of the longitudinal asymmetry in the 0.74-eV p-wave resonance of ^{139}La were carried out at KEK [10, 11]. They obtained the longitudinal asymmetry with respect to the p-wave cross section as $(9.8 \pm 0.3) \times 10^{-2}$ and the value of xW was deduced to be (1.7 ± 0.1) meV. At Los Alamos National Laboratory the TRIPLE collaboration measured longitudinal asymmetries in many p-wave resonances of various nuclei which were in the mass regions of $A \sim 230$ and $A \sim 100$ [12, 13, 14, 15, 16, 17, 18, 19]. They performed analyses based on the s-p mixing model, and studied the weak matrix element xW systematically.

An attempt to measure the neutron spin rotation angle covering the 0.74-eV p-wave resonance of ^{139}La was performed at KEK by Sakai et al. in 1993[20, 21]. They used a polarized proton filter to polarize neutron beam, and a polarized ^3He filter to

analyze the spin direction of the transmitted neutron. They found that the energy dependence of the rotation angle shows a dispersive behavior changing its sign at the center of the p-wave resonance, as expected from the s-p mixing model. They deduced the value of xW to be (1.00 ± 0.37) meV, which is consistent with the result obtained by Heckel et al. who measured the rotation angle using cold neutrons [23]. Assuming that the s-p mixing picture is valid for the tail of the p-wave resonance, xW is estimated to be 1.63 ± 0.21 meV from the data.

Serebrov et al. measured the neutron spin rotation angles at several energies around 0.74-eV with a ^{139}La target at Gatchina [22]. They used a crystal-diffraction method to produce a polarized neutron beam and to analyze the neutron polarization after the target. They also obtained the result that the spin rotation angle shows a dispersion curve.

If we compare the accuracies of these data with those on the longitudinal asymmetry, the experimental data on the spin rotation are still quite poor, particularly for on-resonance measurements. [1] Thus it is desirable to improve the data accuracy to validate the s-p mixing picture from the measurements of both the imaginary and the real parts and to check the consistency between the on- and off-resonance measurements.

1.4 Present Work for the Measurement of the Parity-Nonconserving Neutron-Spin Rotation

The present work has been carried out to obtain the experimental information on the parity-nonconserving neutron spin rotation at the 0.74-eV p-wave resonance of ^{139}La. The experiment was performed at MLNSC (Manuel Lujan Jr. Neutron Scattering Center) in LANSCE (Los Alamos Neutron Science Center). At this facility, the neutron beam is more than 30 times as intense as that of the KEK neutron source.

In Chapter 2, the apparatus and the procedure of the experiment are explained. The analysis of the data is described in Chapter 3. The obtained results are shown in Chapter 4. Chapter 5 gives the conclusion of this work.

[1] It should be noted that Serebrov et al. have been improving the measurement of the spin rotation angle in their previous work [22]. It is expected that the absolute amplitude of the spin rotation will appear soon [24].

Chapter 2

Experimental Procedure

The principle of the present experiment to measure the parity nonconserving rotation angle of neutron spin is shown schematically in Figure 2.1.

We prepared two spin filters, a polarizer and an analyzer, before and after the target, respectively. These polarization axes were transverse to the beam direction and orthogonal to each other. By flipping the spin direction of the polarizer, the neutron transmission became sensitive either a clockwise rotation or a counterclockwise rotation. The difference of the transmissions between these two settings gave the angle of neutron-spin rotation. A schematic view of the experimental apparatus and the beam line is shown in Figure 2.2. In this chapter, detail descriptions of the experimental apparatus are presented.

2.1 Accelerator Complex and Spallation Neutron Source

At MLNSC in LANSCE, neutron beams which cover an energy range from 10^{-4} to 10^{5} eV are available in more than 10 beam lines. The neutron beam is

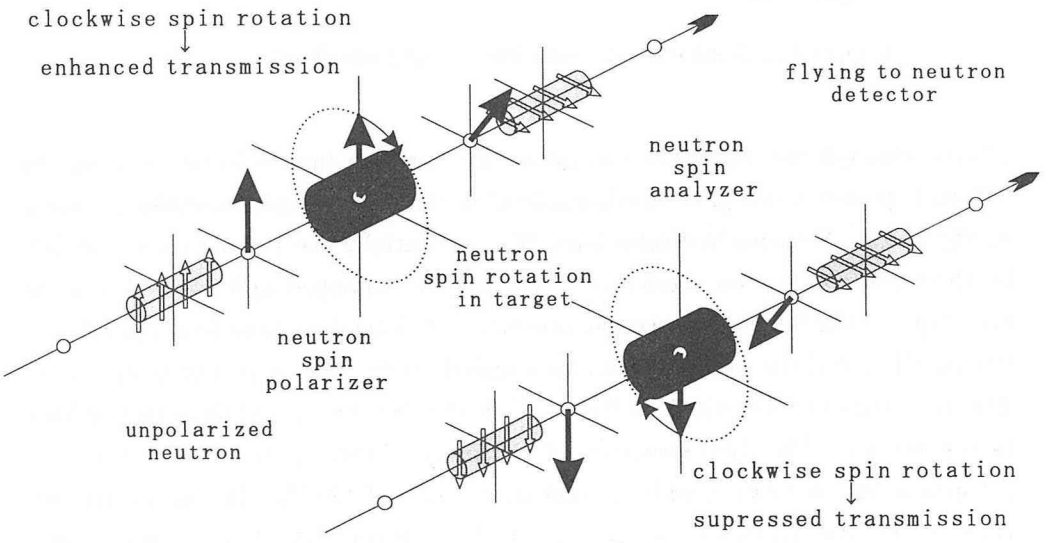

Figure 2.1: A scheme of two configurations of the neutron spin filters.

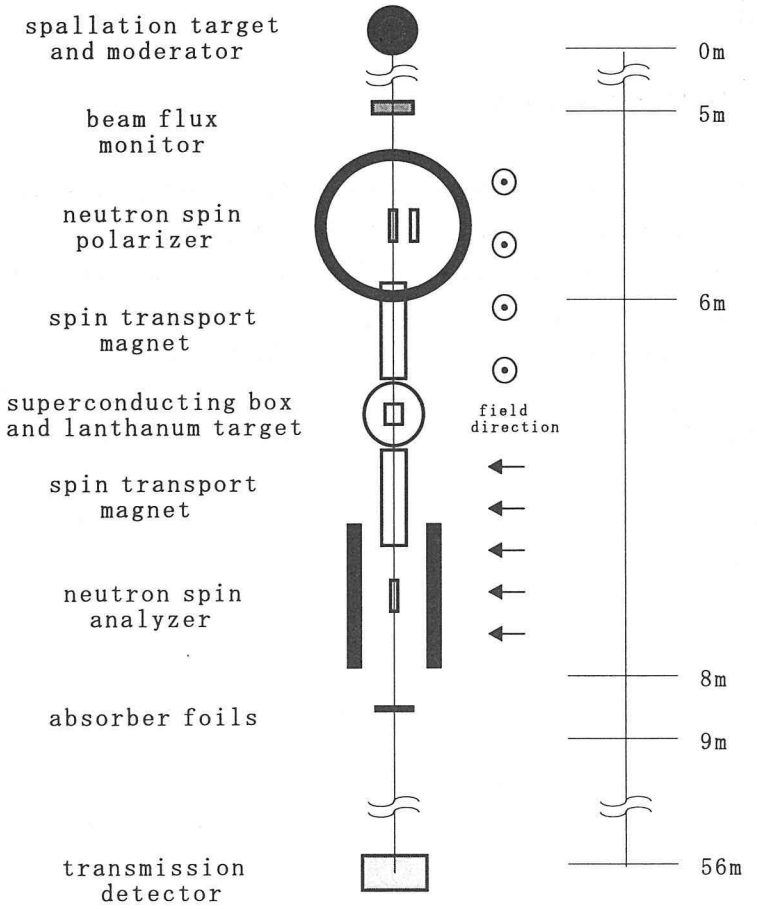

Figure 2.2: A scheme of beam line setup (top view).

created through the spallation process in the tungsten targets bombarded by the 800-MeV proton beam [25]. A schematic view of the accelerator complex is shown in Figure 2.3. Negative hydrogen ions, H^-, are initially accelerated up to 750 keV by the Cockcroft-Walton accelerator. The ions are chopped and injected into the two stages of the linacs downstream, one is a 62-m-long drift-tube linac operated at 201.25 MHz, and the other a 48-sector coupled-cavity linac operated at 805 MHz. The H^- beam is accelerated to 100 MeV in the first linac, and then to 800 MeV in the second. The time structure of the proton beam at the exit of the linac consists of bunches with a width of 800 μs at a rate of 120 Hz. The kicker magnets chop the H^--ion bunches to produce 250-ns-long pulses with 110-ns gaps to deliver them to the PSR(Proton Storage Ring) whose circulation time is 360 ns. A strong

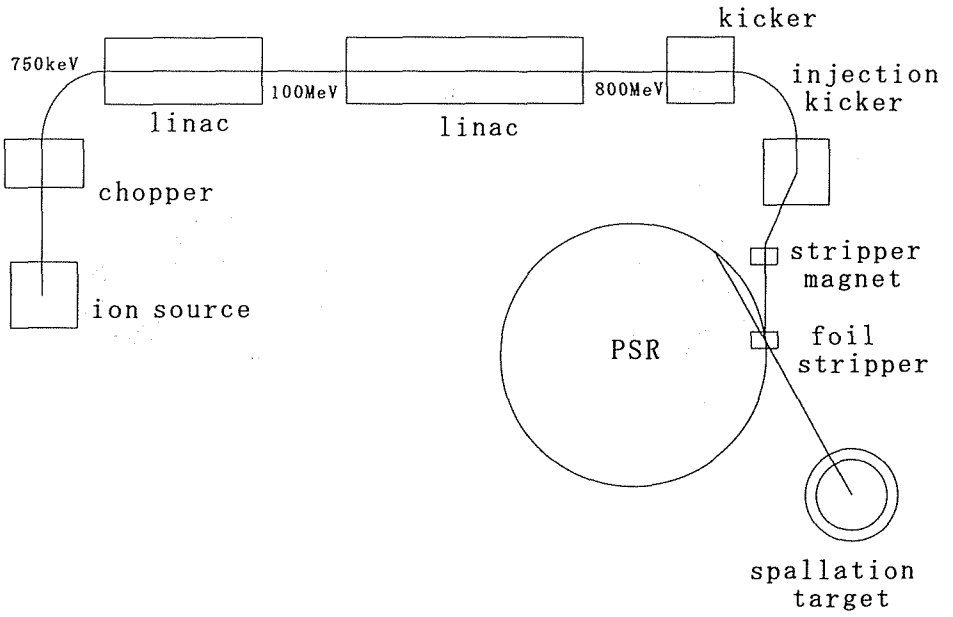

Figure 2.3: A scheme of LANSCE-MLNSC accelerator complex.

transverse magnetic field at the entrance of PSR removes one electron from H^- ion and the second electron is removed by a carbon foil of 200 μg/cm^2 located in the PSR ring. The neutral injection scheme to PSR is essential in order to produce a intense pulsed proton beam. The beam bunches delivered from the linac are stacked on the circulating bunch in the ring at the location of the carbon foil.

The PSR accumulates the proton beam for about 450 μs stacking 1250 beam bunches from the kickers. The bunch shape in PSR is an isoscale triangle whose base is 250 ns. The proton current delivered to the spallation target is usually about 70 μA with a repetition rate of 20 Hz. Thus about 2×10^{13} protons are transported in a single bombardment to the target vertically from the top.

The spallation target consists of two cylinders made of tungsten oriented vertically as shown in Figure 2.4. The upper piece is 10 cm in diameter and 7.25 cm in length, the lower is 10 cm in diameter and 27 cm in length, and they are separated by 14 cm. There are four moderators around the gap, the size of each is 13 cm $\times$ 13 cm. Three of them are made of water and one is made of liquid hydrogen. The γ-ray background in the beam line is greatly reduced in such a "flux-trap" geometry. The moderators are cylindrically surrounded with a beryllium reflector. About 17 neutrons for each incident 800-MeV proton are produced in the spallation process.

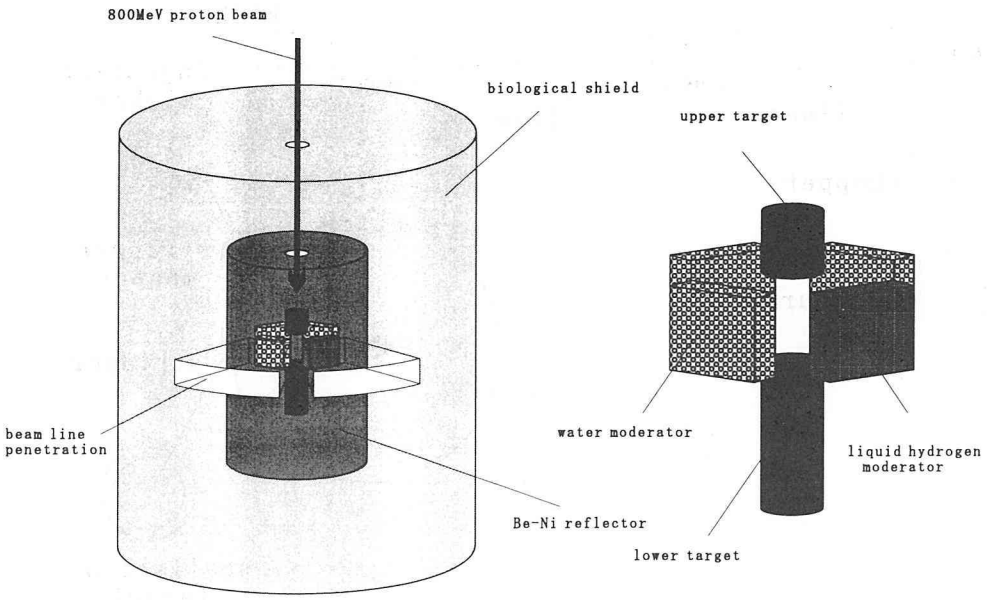

Figure 2.4: A schematic view of the spallation target.

The energy distribution of the neutrons has a peak at about 2 MeV. Energy of them are reduced into the epithermal range by the moderators and the extracted neutron beam has a peak at about 40 meV in the energy distribution.

According to the measurement of the neutron flux emerged from the moderator [26], the energy distribution of the neutrons per bunch, $\frac{\Delta N}{\Delta E}$ is given as

$$\frac{\Delta N}{\Delta E} = 5.8 \times 10^{-3} \frac{1}{E^{0.9}} w f \Omega \ , \tag{2.1}$$

where w, f, and Ω are the number of protons in a single bunch, the fraction of the moderator viewed from the detector, and the solid angle covered by the detector, respectively. And E is the energy of neutron in the unit of eV.

2.2 Neutron Flux Monitor

In order to measure the neutron flux, a beam monitor was installed after the biological shield. The beam monitor was the most upstream detector in the experiment.

The beam monitor consisted of a pair of ion chambers. A schematic view of each chamber is shown in Figure 2.5. One was filled with ^3He gas, and the other

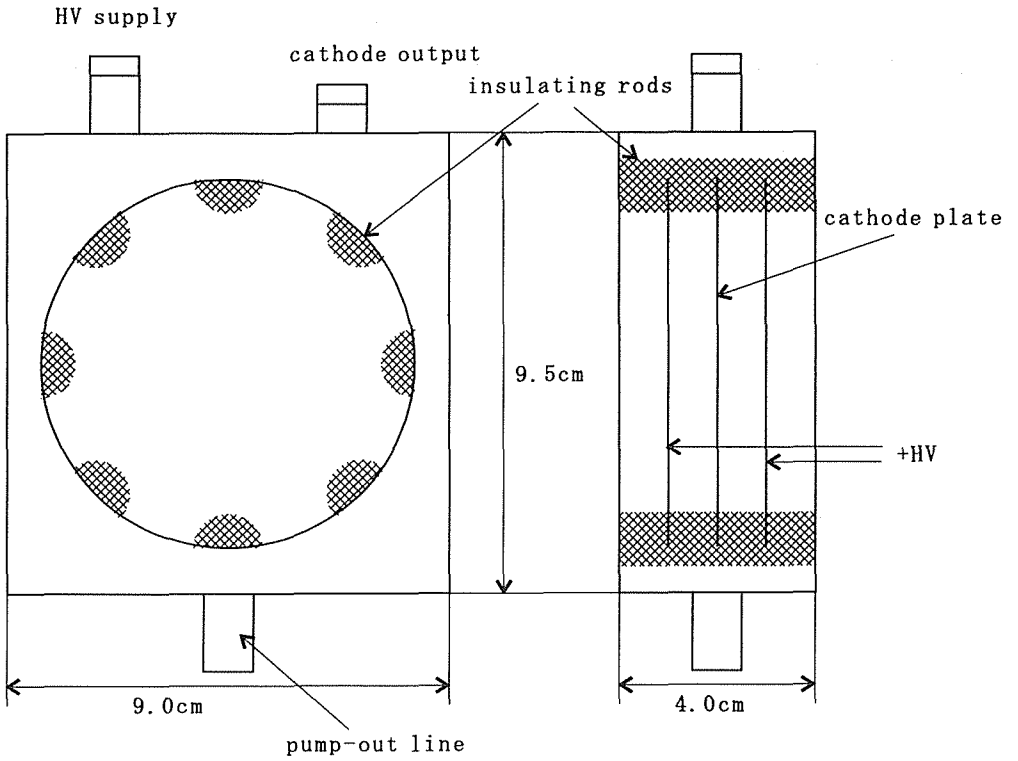

Figure 2.5: Ion chamber used for the beam monitor as a pair.

with ^4He gas. Both of the chambers were operated at 1 atm of gas pressure. Each chamber had a charge collection plate at its center, which was sandwiched between two anode plates where high voltage of +600 V was applied [27]. The sensitive thickness between the two anodes was 2 cm.

The ^3He chamber had sensitivity to neutrons through the reaction,

$$n + {}^3He \rightarrow p + {}^3H + 0.764\,\mathrm{MeV}\ , \tag{2.2}$$

while the ^4He chamber was insensitive to neutrons. A small fraction of neutrons passing through ^3He gas was absorbed and created ions in the ^3He chamber. On the other hand, both of the ion chambers had sensitivity to γ-rays because of the interactions with the aluminum windows and the gas.

The current signal from each chamber was converted to the pulse signal with a voltage-to-frequency converter, and sent to a scaler in the data acquisition room. The number of the pulses proportional to the neutron intensity was obtained by subtracting that of ^4He chamber from that of ^3He chamber. In order to cancel

the noise signal caused by the AC power supply of 60 Hz, the measurement were repeated 1/60 second after each bombardment, and an electric noise component was subtracted. It was examined that this system did not have a fluctuation caused by the change of magnetic field and temperature [27].

2.3 Neutron Spin Polarizer

In order to polarize the neutron beam, polarized ^3He gas was used as a polarizer in the present experiment. Since the n–^3He cross section is essentially all associated with a 0^+ compound state [28], the polarized ^3He nuclei absorb only neutrons whose spins are antiparallel to the ^3He spin. The cross section follows the "$1/v$-rule", and is $(5,327 \pm 10)$ barns at 25.3 meV [29].

In the polarizer two cylindrical glass cells whose inner sizes were 10 cm in length and 30 mm in diameter were used. One containing a small amount of rubidium and 100 Torr of nitrogen in addition to ^3He gas was called "real cell" and the other containing neither rubidium nor nitrogen was called "dummy cell" and placed 107 mm away from the real cell. ^3He gas was filled at a pressure of 6 atm in the real cell and 3 atm in the dummy cell. The pressure of 6 atm in the real cell was chosen to be optimum for asymmetry measurements for neutrons of 0.74 eV determined by the polarization and the transmission. The polarizer was mounted on a movable table so that both cells could be alternately set on the neutron beam path. The dummy cell was used only for the measurement of the analyzing power of the spin analyzer as described in Section 3.2.4. The movable table was attached on a "gimbal" mount which could rotate the whole ^3He polarizer around the center of the beam path. The direction of the polarization was set vertical during the measurement of the spin rotation angle. The direction was kept to horizontal during the measurements of the analyzing power.

Polarization of ^3He nuclei was obtained via optically pumped Rb atoms. Irradiation of circularly polarized photon polarizes the Rb atoms, which is transfered to the ^3He nuclei by diffusion. Details of the mechanism are described in Appendix A. For optical pumping, two sets of fiber-coupled diode-laser arrays were used. The laser optics of the polarizer system is schematically shown in Figure 2.6.

Using AFP-NMR (Adiabatic Fast Passage Nuclear Magnetic Resonance), the

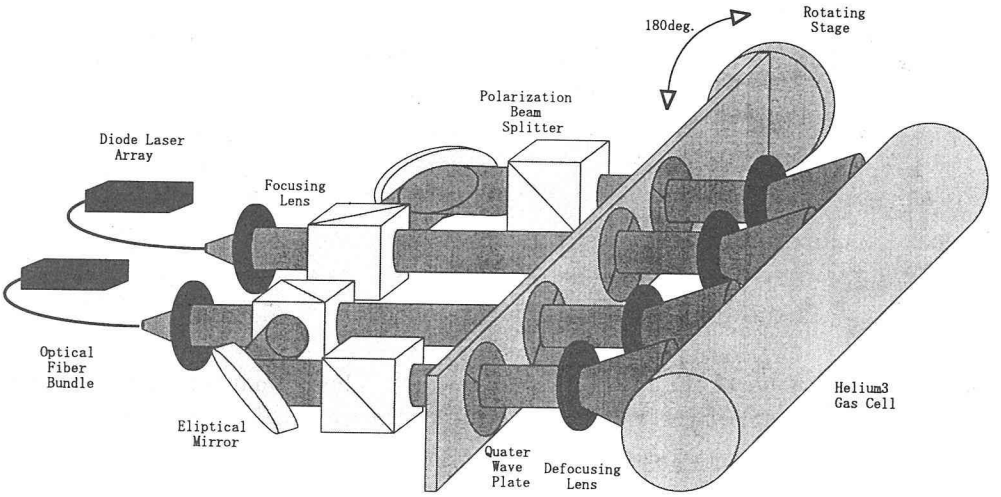

Figure 2.6: A scheme of the laser optics in the polarizer.

polarization vector of ^3He nuclei was flipped. The mechanism of AFP-NMR is explained in Appendix B. Flipping of the polarization of ^3He by means of AFP-NMR makes the polarization of ^3He nuclei and Rb atoms antiparallel to each other and causes depolarization of the ^3He nuclei. In order not to reduce the ^3He polarization, the quarter wave plates were turned over simultaneously with the flipping. AFP-NMR was also used to monitor the polarization of ^3He.

2.4 Upstream Spin Transport Magnet

In order to hold the spin vectors of the beam neutrons, a spin transport magnet of 84 cm in length was placed downstream the polarizer. The magnet consisted of a pair of race-track-type coils and a return yoke, and with two permanent magnets of about 160 gauss at the both ends. Figure 2.7 shows a schematic view of the spin transport magnet. The magnet was rotatable around the beam direction in order to keep the same field direction as the polarizer. The field strength of the electromagnet was usually 38 gauss and it was reduced to 29 gauss for a short period of the experiment. The permanent magnet placed at the upstream end was removed during the weak field measurement, which was carried out for checking the systematic error caused by the magnetic field in the beam line. The magnet was

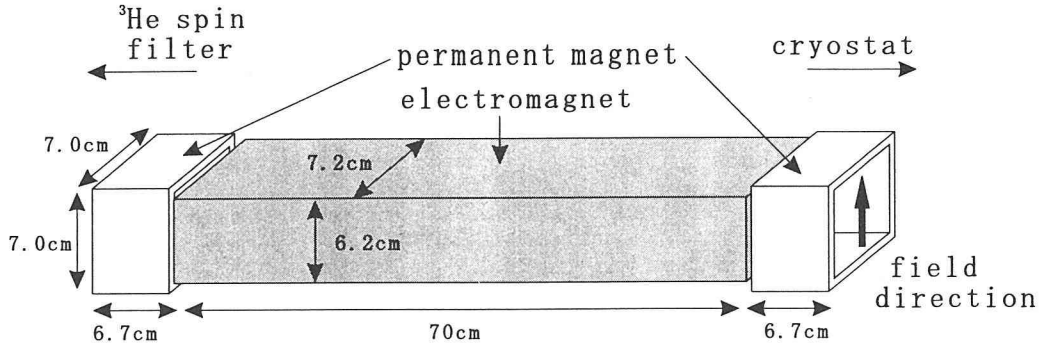

Figure 2.7: A scheme of the spin transport magnet. The permanent magnet placed nearer to the ^3He spin filter was removed during the weak field measurement.

also slidable in the beam direction. During the data taking the magnet was closely attached to the entrance window of the target cryostat. The magnet was slided out in order to make an insertion space for magnetic shield of the cryostat when we cooled down the target cryostat.

2.5 Lanthanum Target and Superconducting Magnetic Shield

Since neutron spin is subject to rotating by any residual magnetic field, the shielding of the magnetic field around the target was one of the essential points in this experiment. On the other hand, to keep the neutron spin components of interest, applying transverse magnetic field upstream and downstream of the target, whose directions were perpendicular to each other, was also essential. In order to satisfy the both requirements, the ^{139}La target was installed in the superconducting box, which was a niobium cylinder of 10 cm in diameter, 60 cm in length, 0.3 mm in thickness and niobium lids of the same thickness at the both ends of the cylinder. Figure 2.8 illustrates the structure of the cryostat. Penetration of magnetic field was greatly suppressed owing to the Meissner effect, and a space without magnetic field is realized inside the superconducting box.

Since niobium becomes superconducting below 9.2 K, the superconducting box was cooled down to the liquid helium temperature in the cryostat. The superconducting box was placed at the lower part of the cryostat. The upper part of the cryostat consisted of two reservoirs. One was for liquid helium and the other for

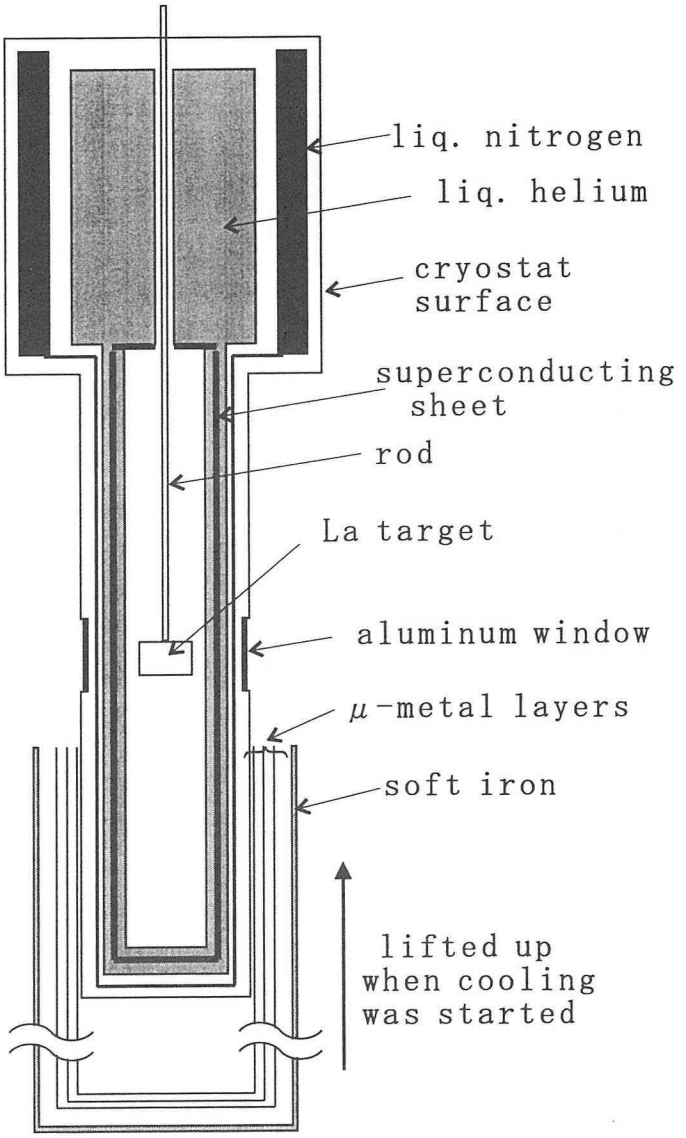

Figure 2.8: A scheme of the cryostat.

liquid nitrogen. Liquid nitrogen was used only for cooling the insulating part in order to reduce consumption rate of liquid helium.

When cooling of the superconducting box was started, the lower part of the cryostat was covered with a cylindrical magnetic shield consisted of three-layered μ-metal sheet and single-layered soft iron sheet. The bottom end of the cylindrical

shield was closed while the other open. The thicknesses were 1 mm for each μ-metal layer and 6 mm for the soft iron layer. Upstream and downstream surfaces of the cryostat were plain windows made of aluminum, where the neutron beam passed through.

A lanthanum target of a cylindrical shape of 30 mm in diameter, 50 mm in length was placed in the superconducting box. The target was suspended by a rod from the top of the cryostat and was able to be lifted up in order to compare the neutron transmissions with the target and without the target.

2.6 Downstream Spin Transport Magnet

In order to keep the spin component resultant from the spin rotation and to transfer it to the neutron spin analyzer, the second spin transport magnet was placed downstream of the cryostat. The magnet had the same structure as the upstream one in Figure 2.7, but it could not be rotated around the beam direction. The support was slidable along the beam direction as the upstream transport magnet.

The coils of the downstream and the upstream transport magnets were serially connected to a power supply, to ensure the same field strength in the two transport magnets. During the weak field measurement, the permanent magnet placed at the downstream end was removed.

2.7 Neutron Spin Analyzer

The neutron spin analyzer was placed just after the downstream spin transport magnet. The Helmholtz coils gave the horizontal magnetic field transverse to the beam line, which works as a holding field of the polarization of ^3He nuclei in the cell.

In the analyzer, only one cylindrical glass cell was used. The inner size was 10 cm in length and 30 mm in diameter. It contained ^3He gas at a pressure of 6 atm, nitrogen gas of about 90 Torr, and a small amount of rubidium.

A scheme of the laser optics is shown in Figure 2.9. Direct laser beams from two sets of the diode-laser arrays passed through cylindrical lenses in order to make vertical focusing. The quarter wave plates were inserted after the lenses to obtain circular polarization.

The measurements of AFP-NMR for the ^3He nuclei in the analyzer were done likewise as the polarizer to monitor the polarization of the ^3He nuclei. The polarization of the ^3He nuclei in the analyzer was not flipped during the experiment.

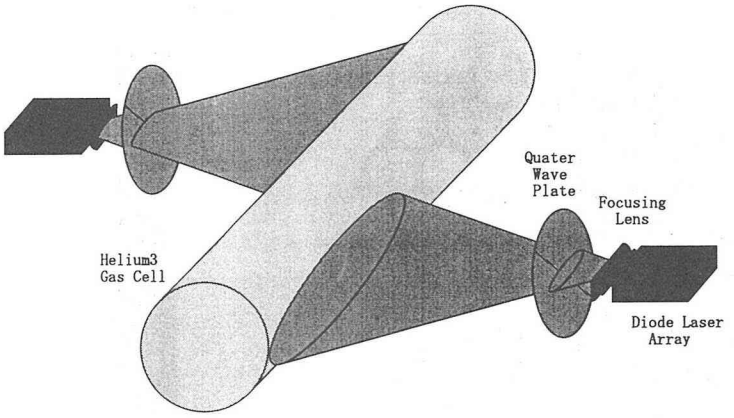

Figure 2.9: A scheme of the laser optics in analyzer.

2.8 Neutron Absorber Foils

Neutron absorber foils were occasionally inserted in the beam line downstream the neutron spin analyzer. The purpose of the absorber foils was to measure the γ-ray background levels in the beam. Three types of materials, tantalum, indium, and cadmium were used. Each material has a strong resonance so that even with a thin foil neutrons around the resonance energy were either absorbed or scattered completely. Two foils with different thicknesses for each material were used in order to estimate the background of the γ-rays without the absorbers. Detailed procedures are described in the next chapter. The absorber foils were packed between two aluminum plates. During the measurements of the rotation angle, an empty holder made of the aluminum plates was placed. All the foils and the empty holder were mounted on a wheel which could be rotated remotely by a stepping motor.

2.9 Neutron Transmission Detector

The neutron transmission detector was placed 48-m downstream of the neutron spin analyzer. The detector consisted of segmented ^{10}B-loaded liquid scintillator and 55 photomultiplier tubes[30]. The liquid scintillator was filled in a volume of a cylindrical shape of 43 cm in diameter and 4 cm in thickness, and segmented in a honeycomb pattern. A schematic view of the detector is shown in Figure 2.10. Each segment was read out by Amprex XP2262B, a photomultiplier tube of 2 inches in diameter.

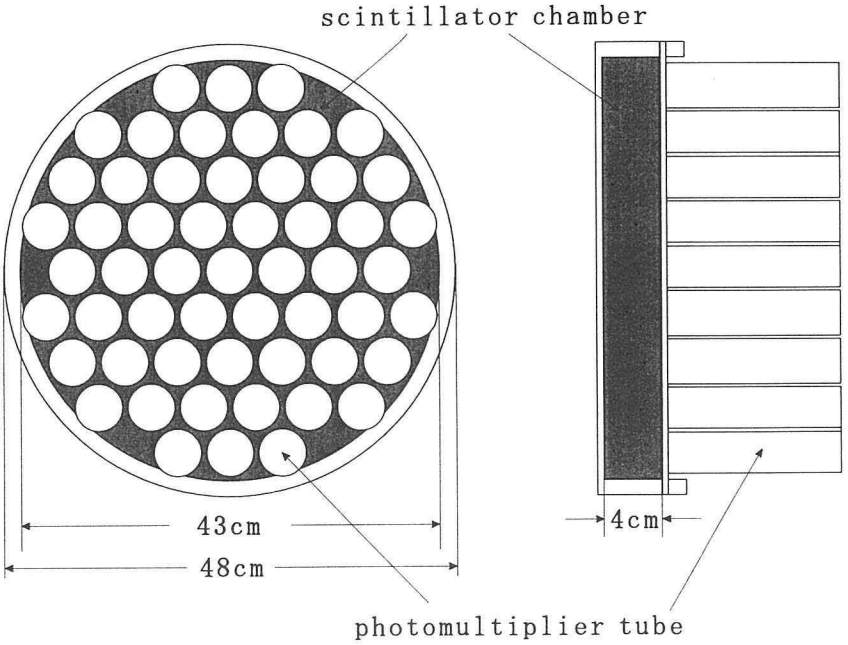

Figure 2.10: A schematic view of the transmission detector.

Most of the neutrons entering into the scintillator were moderated to thermal energies and then captured by ^{10}B nuclei through the following reactions,

$$\begin{aligned} n + {}^{10}B \rightarrow\ & {}^{7}Li^{*} + \alpha + 2.310\,\mathrm{MeV} \\ & \downarrow \\ & {}^{7}Li\ + \gamma(0.482\,\mathrm{MeV})\ . \end{aligned}$$

The α-particle, the ^{7}Li-nucleus, and the γ-ray, which were released in the above reaction, excited molecules in the scintillator. Resulting scintillation photons were detected by the photomultiplier tubes. The detection efficiency for neutrons was nearly 100% up to 1 keV. Owing to the segmentation, high instantaneous counting rates as high as 500 MHz were acceptable. An anode output of each photomultiplier tube was filtered with a time constant of 5 ns and discriminated. The signal was sent to the data room via a cable of about 150 m long and there reshaped again with a discriminator.

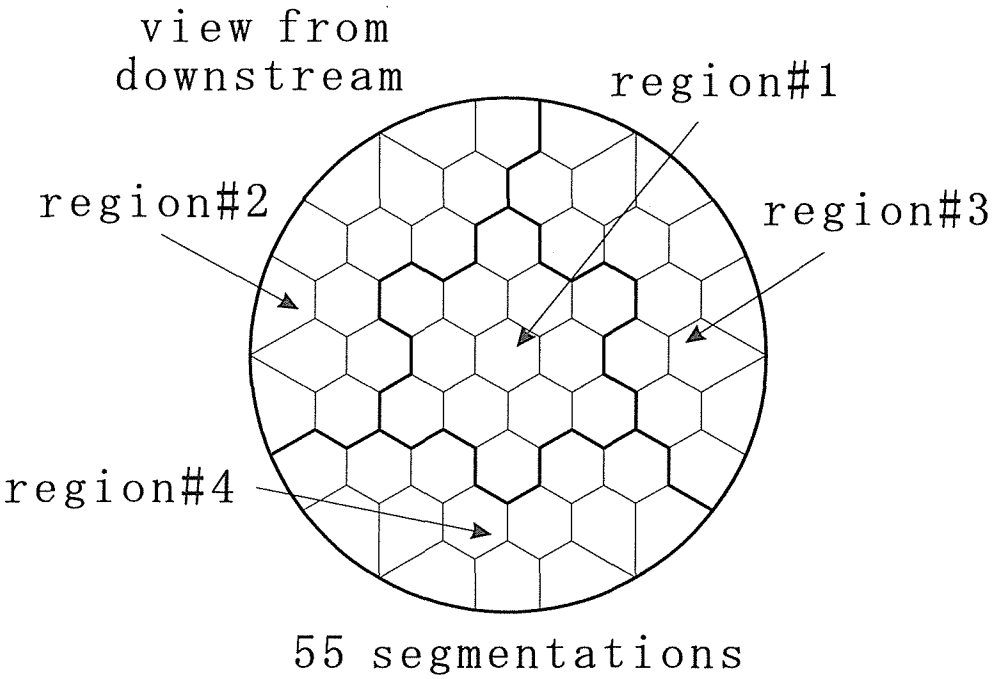

Figure 2.11: Summation regions of the detector segmentation.

2.10 Data Taking

The data acquisition system consisted of electronics modules of the VME and the CAMAC standards, which were controlled by a UNIX workstation. The data acquisition system was triggered by the 20 Hz signal defined by the timing when the proton beam bombarded the spallation target.

The reshaped pulses of the 55 discriminator outputs which were sent from the transmission counter to the data room were summed up into 4 NIM-logic signals. The NIM signals corresponded to the summation regions as shown in Figure 2.11. Each NIM logic signal was sent to a multi channel scaler (MCS), Turbo-MCS T914 (EG&G ORTEC), whose dwell time was set at 1 μs with an external timer which was started by the trigger signal induced by the proton beam. The MCS counted the signals until 9625 μs from the trigger, then returned to the first bin to wait for the next beam burst.

In the measurements of the rotation angle, we repeated the runs accumulating the data for 4800 beam bursts followed by the polarization flipping of the ^3He spin polarizer. In the measurements of the analyzing powers of the polarizer and the

analyzer, the data accumulation continued for 2400 beam bursts, then the mounting table of the polarizer was moved to exchange the real and the dummy cells.

The AFP-NNR signals of the two polarized ^3He systems was monitored by another personal computer remotely controlled by the UNIX workstation. The personal computer had a 4-channel ADC. The amplitude of the NMR signal and its phase with respect to the RF were obtained using a lock-in amplifier. The output wave forms of the lock-in amplifier were recorded with sampling ADCs in the personal computer.

Chapter 3

Analysis

The procedure of the data analysis is described in this chapter. In the first section, we present mathematical formulae describing how the effect of the rotation angle appears and how the rotation angle is extracted from the neutron transmission spectra. In the second section, the detail procedure of the data analysis is described. Although the neutron transmission data were taken with 4 MCSs, due to the low statistics of the peripheral regions, only the data corresponding to the central region of the detector array were used in the analysis.

3.1 Analysis Formulae

3.1.1 Transmission of Neutrons through Polarized ^3He Nuclei

Since the reaction of epithermal neutron and ^3He nucleus occurs when their spins are antiparallel to each other, the cross section can be regarded as zero when the spin components is parallel to each other, while it can be regarded as $2\sigma_{^3He}$ when they are antiparallel, where $\sigma_{^3He}$ represents the unpolarized cross section for neutrons on ^3He nucleus.

Thus the transmission of neutrons whose spin component is parallel to the ^3He polarization, T^+, (or antiparallel, T^-) is calculated as

$$T^{\pm}(P_{^3He}, \varrho_{^3He}) = \exp\left(-\frac{(1 \pm P_{^3He})}{2}\varrho_{^3He}\sigma_{^3He}\right) , \tag{3.1}$$

where $P_{^3He}$ is the polarization of the ^3He nuclei, and $\varrho_{^3He}$ is the product of the

nuclear number density and the length of the ^3He gas. Through the spin filter the neutron beam becomes polarized and its polarization P_n^{pol} is given as

$$\begin{aligned} P_n^{pol} &= \frac{T^+(P_{^3He}, \varrho_{^3He}) - T^-(P_{^3He}, \varrho_{^3He})}{T^+(P_{^3He}, \varrho_{^3He}) + T^-(P_{^3He}, \varrho_{^3He})} \\ &= \tanh\left(P_{^3He}\varrho_{^3He}\sigma_{^3He}\right) \ . \end{aligned} \tag{3.2}$$

If the incident neutrons are polarized, the transmission through the polarized ^3He gas is calculated similarly as

$$\begin{aligned} T(P_n, P_{^3He}, \varrho_{^3He}) &= \frac{1+P_n}{2}T^+(P_{^3He}, \varrho_{^3He}) + \frac{1-P_n}{2}T^-(P_{^3He}, \varrho_{^3He}) \\ &= \cosh\left(P_{^3He}\varrho_{^3He}\sigma_{^3He}\right) + P_n \sinh\left(P_{^3He}\varrho_{^3He}\sigma_{^3He}\right) \ , \end{aligned} \tag{3.3}$$

where P_n stands for the polarizations of the incident neutron beam.

The flipping ratio F is defined as the asymmetry of the transmissions for the flipping of incident neutron polarization. The F is derived as

$$\begin{aligned} F &= \frac{T(P_n, P_{^3He}, \varrho_{^3He}) - T(-P_n, P_{^3He}, \varrho_{^3He})}{T(P_n, P_{^3He}, \varrho_{^3He}) + T(-P_n, P_{^3He}, \varrho_{^3He})} \\ &= P_n \tanh\left(P_{^3He}\varrho_{^3He}\sigma_{^3He}\right) \ . \end{aligned} \tag{3.4}$$

Now we consider the configuration of the experiment. The ^3He gas in the polarizer is polarized vertically, and the analyzer is polarized horizontally. The incident unpolarized beam is polarized after the polarizer. The polarization P_n^{pol} is given as

$$P_n^{pol} = \tanh\left(P_{pol}\varrho_{pol}\sigma_{^3He}\right) \ , \tag{3.5}$$

where the subscript of *pol* is for the polarizer.

We consider that the neutron polarization vector is rotated by an angle θ between the polarizer and the analyzer. Then the polarization of neutron beam entering the analyzer can be considered as $P_n^{pol}\sin\theta$. By flipping the polarization of the polarizer, we observe the flipping ratio as

$$F = P_n^{pol}\sin\theta\tanh\left(P_{ana}\varrho_{ana}\sigma_{^3He}\right) \tag{3.6}$$

$$= \sin\theta\tanh\left(P_{pol}\varrho_{pol}\sigma_{^3He}\right)\tanh\left(P_{ana}\varrho_{ana}\sigma_{^3He}\right) \ , \tag{3.7}$$

where the subscript *ana* is for the analyzer. The rotation angle, $\sin\theta$, is obtained by the normalized projection asymmetry A as

$$A = \sin\theta = \frac{F}{\tanh\left(P_{pol}\varrho_{pol}\sigma_{^3He}\right)\tanh\left(P_{ana}\varrho_{ana}\sigma_{^3He}\right)} \ . \tag{3.8}$$

3.1.2 Asymmetry due to Spin Rotation Angle and Residual Magnetic Field

Besides the spin rotation caused by the neutron-^{139}La interaction, the residual magnetic field in the beam line can produce a fake spin rotation. The effect of the residual field can be measured by the empty runs, namely;

$$\theta^{empty} = \phi_{mag} \quad (\text{ target is removed from the beam }) \tag{3.9}$$

$$\theta^{La} = \phi_{sr} + \phi_{mag} \quad (\text{ target is in the beam }) \tag{3.10}$$

where ϕ_{mag} and ϕ_{sr} is the neutron spin rotation angle caused by the residual magnetic field and ^{139}La nucleus, respectively. Since ϕ_{mag} and ϕ_{sr} are small enough, we can take approximations as $\sin\phi_{mag} \simeq \phi_{mag}$ and $\sin(\phi_{sr} + \phi_{mag}) \simeq \phi_{sr} + \phi_{mag}$. Thus the rotation angle caused by ^{139}La nucleus can be simply extracted as following,

$$\phi_{sr} \simeq A^{La} - A^{empty} , \tag{3.11}$$

where A^{La} and A^{empty} are the normalized projection asymmetries measured with and without the target, respectively.

In order to calculate A^{La} and A^{empty}, the terms, $P_{pol}\varrho_{pol}\sigma_{^3He}$ and $P_{ana}\varrho_{ana}\sigma_{^3He}$, have been experimentally deduced by means of the transmission enhancement method. Considering the situation that a beam of unpolarized neutrons passes through ^3He gas in either the polarizer or the analyzer, the transmission enhancement T_E is defined as a ratio of the transmission through the polarized ^3He gas to that through the unpolarized ^3He gas,

$$\begin{aligned} T_E(P_{^3He}, \varrho_{^3He}) &= \frac{T(0, P_{^3He}, \varrho_{^3He})}{T(0, 0, \varrho_{^3He})} \\ &= \cosh(P_{^3He}\varrho_{^3He}\sigma_{^3He}) . \end{aligned} \tag{3.12}$$

This means that the transmission becomes larger when the polarization increases, and the values $P_{pol}\varrho_{pol}\sigma_{^3He}$ and $P_{ana}\varrho_{ana}\sigma_{^3He}$ can be deduced by the measurements of transmission enhancements for both the polarizer and the analyzer. The normalized projection asymmetry defined in Equation (3.8) is thus obtained from the measurement of the flipping ratio, F.

3.2 Data Analysis

3.2.1 Determination of Kinetic Energies of Neutrons in Beam

In order to determine the kinetic energy of beam neutrons, we have applied the time-of-flight (ToF) method, which uses a relation between the velocity and the ToF of a neutron to pass 56 m down to the transmission counter. In Equation(3.13), the energy of the neutron, E_n, is related to the flight length, L, and the ToF, t, as

$$E_n = \frac{1}{2} m_n v_n^2 = \frac{1}{2} m_n \frac{L^2}{t^2} \ , \tag{3.13}$$

where m_n and v_n are the mass and the velocity of the neutron, respectively. Since there was a timing offset t_0 on the multi channel scaler (MCS), the ToF, T, measured with MCS was related to t and t_0 as

$$T = t + t_0 \ . \tag{3.14}$$

Combining Equations (3.13) and (3.14),

$$E_n = \frac{m_n}{2} \frac{L^2}{(T - t_0)^2} \tag{3.15}$$

is obtained.

We determined L and t_0 using the resonances of known energies listed in Table 3.1. The result is shown in Figure 3.1. The beam line length, L, obtained from the fitting was $L = (56.22 \pm 0.22)$ m .

The precision of the ToF calibration was 5.5 meV, which was limited by the precision of the resonance energies in the litratures, but it was precise enough for the present experiment.

nucleus	resonance energy(eV)
^{139}La	0.734 ± 0.005
^{163}Dy	1.713 ± 0.004
^{138}La	2.99 ± 0.01
^{161}Dy	3.68 ± 0.03
^{162}Dy	5.44 ± 0.02
^{115}In	9.07 ± 0.04
^{181}Ta	13.95 ± 0.05

Table 3.1: The resonance energies used for the ToF calibration.[31]

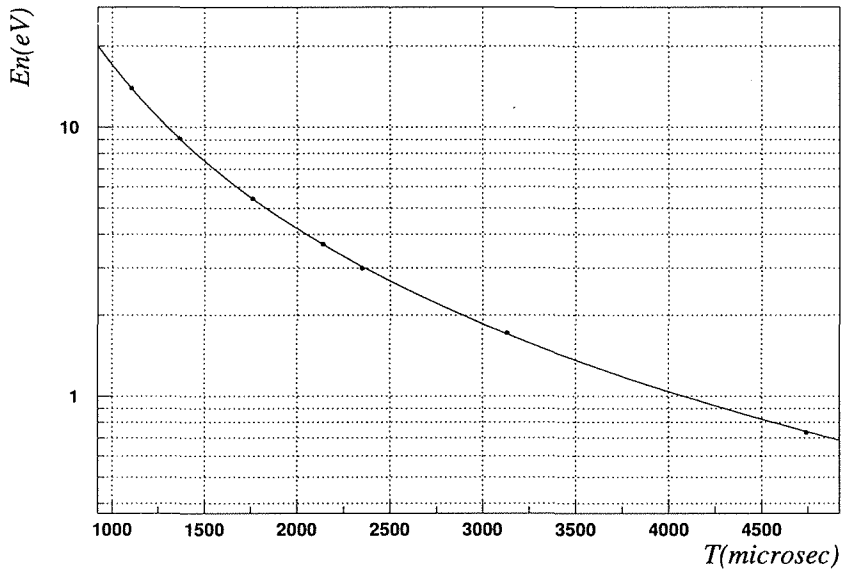

Figure 3.1: Relation between ToF and neutron energy. The line is the obtained calibration curve.

3.2.2 Analysis of NMR Signals

Although the transmission enhancement method provided all the coefficients needed to obtain the rotation angle, the NMR signals were sequentially measured to compensate run by run fluctuations of the ^3He polarizations.

The NMR data taken in the experimental period is plotted in Figure 3.2. In the plot, the vertical axis is the area of the NMR pulse signal in arbitrary unit and the horizontal axis is the date when the NMR signals were taken. The jumps seen in the NMR signals of the polarizer (Figure 3.2 (A)) were attributed to the change of the NMR sensitivity caused by the rotation of the gimbal mount, or to the build up of the polarization while the neutron beam was off. It has been observed that the NMR signal form is different between the two gimbal mount settings. So it is natural to assume the NMR sensitivity was different between the two settings. In order to estimate the difference, we have compared the NMR strength between before and after the rotations. The obtained ratio, the vertical setting over the horizontal setting, has been within $0.978^{+0.043}_{-0.031}$ from the minimum to the maximum. The observed NMR strength were compensated by this ratio to obtain the run-by-

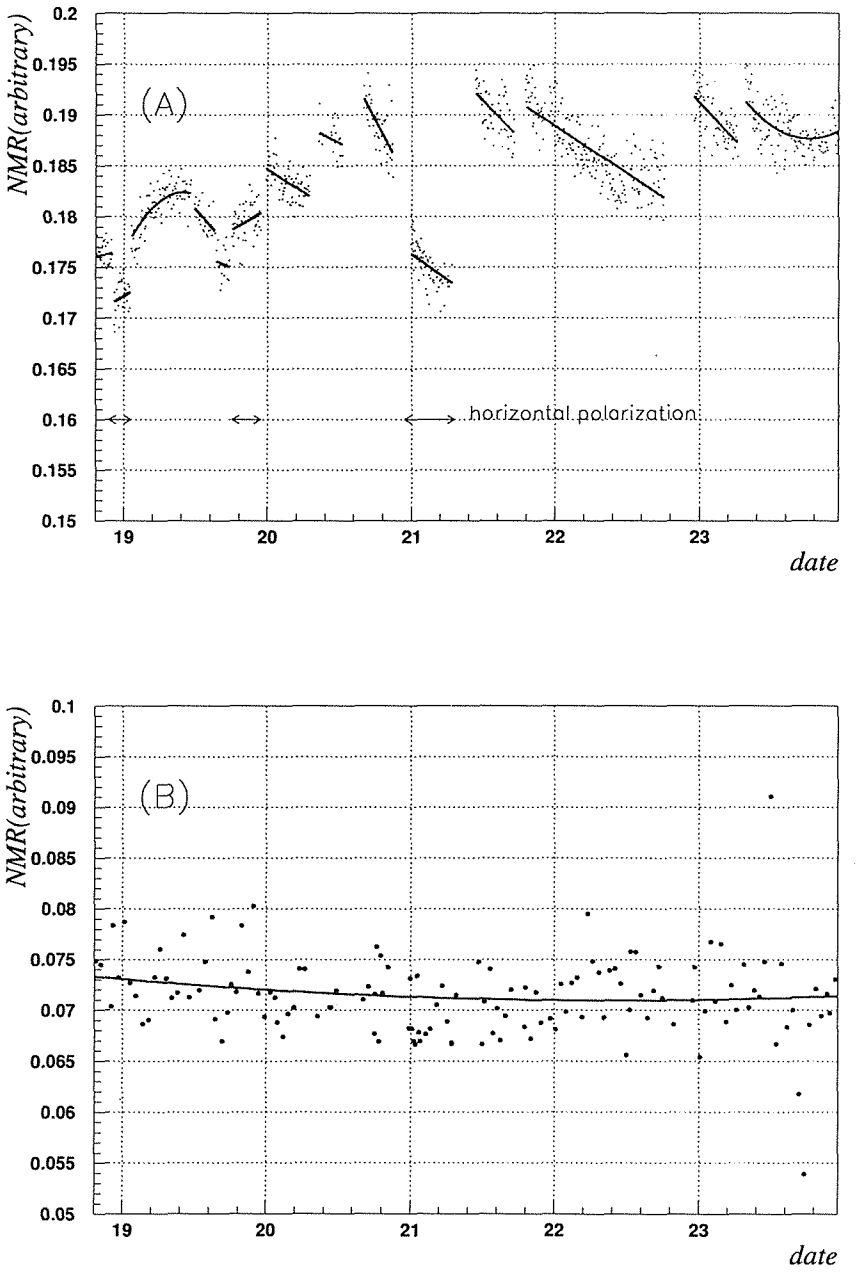

Figure 3.2: NMR signals versus date. The upper figure (A) is for the polarizer. The lower one (B) is for the analyzer.

run changings of the polarization. These phenomena, however, caused the major source of the systematic errors to obtain the spin rotation angle, as described in Section 3.2.6 .

For the analyzer, no significant jumps in the NMR signal have been seen (Figure 3.2 (B)).

3.2.3 Background Estimation in Neutron Transmission

The neutron time spectra, which was measured with the transmission detector, contained the γ-ray background which also has a time dependent shape. In order to estimate the background level, the neutron transmissions with thin absorber foils made of cadmium, indium or tantalum were measured.

The foils used in the measurements are listed in Table 3.2. Since the resonances, 0.18 eV of ^{113}Cd, 1.46 eV of ^{115}In and 4.3 eV of ^{181}Ta, are strong enough, even the thin foil absorbs almost all of the neutron beam around the resonance energy (black region). The thicker foil is twice as thick as the other as listed in the Table 3.2. The foils of both thicknesses were used in the background measurements without the lanthanum target, while only the thinner foils were used with the target.

The yields within the black regions were normalized with the beam flux monitor and the widths of the black regions. Thus we have obtained the normalized yield rates, B_{1T}^{empty}, B_{2T}^{empty}, and B_{1T}^{La}, where the superscripts of La and $empty$ denote the data taken with and without the target, respectively, and the subscripts of $1T$ and $2T$ denote the thinner and the thicker foil, respectively.

The following relations are apparent;

$$B_{1T}^{La} = B_{0T}^{La} e^{-n\sigma t} \tag{3.16}$$

$$B_{1T}^{empty} = B_{0T}^{empty} e^{-n\sigma t} \tag{3.17}$$

$$B_{2T}^{empty} = B_{0T}^{empty} e^{-2n\sigma t} \tag{3.18}$$

where $n\sigma t$ is an attenuation rate of γ-rays in each thinner foil. The γ-ray background rates without the absorbers, B_{0T}^{La} and B_{0T}^{empty} are obtained by the extrapolation as follows;

material of foil	thickness(mm)		resonance energy(eV)	ToF region (μs)
Cd	1.5	3.0	0.18	7000 to 7600
In	0.127	0.254	1.46	3350 to 3500
Ta	1.27	2.54	4.3	1960 to 2010

Table 3.2: Thicknesses of the absorber foils and their black regions.

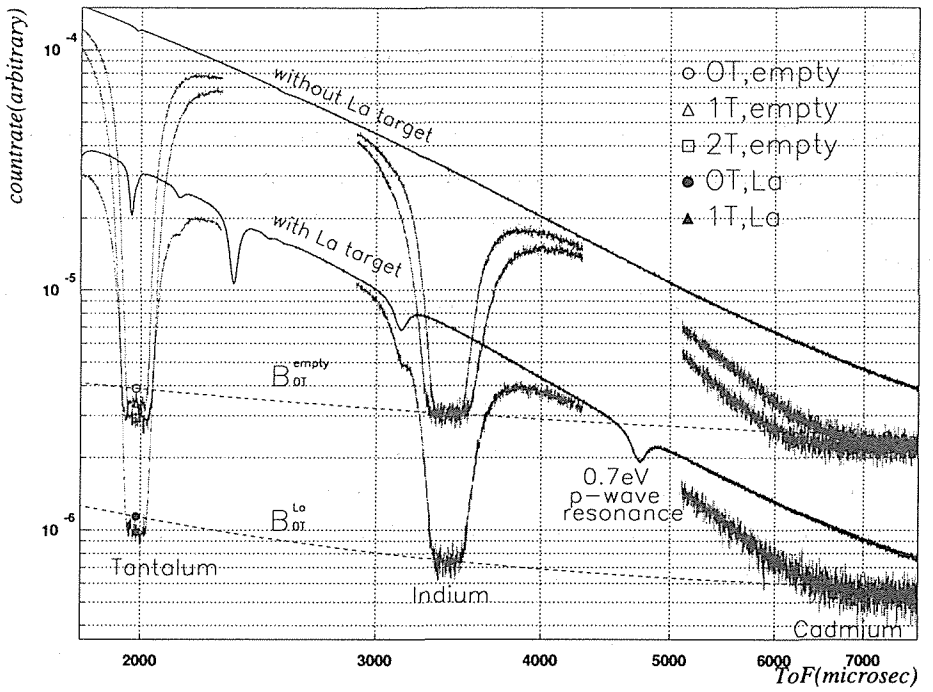

Figure 3.3: Estimation of the ToF dependence of the background. The dashed lines are the best fit on B_{0T}^{La} and B_{0T}^{empty} for the three resonances.

$$B_{0T}^{La} = B_{1T}^{La} B_{1T}^{empty} / B_{2T}^{empty} \tag{3.19}$$

$$B_{0T}^{empty} = B_{1T}^{empty^2} / B_{2T}^{empty} \ . \tag{3.20}$$

$$\tag{3.21}$$

We have obtained B_{0T}^{La} and B_{0T}^{empty} in the three black resonances. The ToF dependence of the background levels is estimated with interpolating the three black resonances. For the interpolation, we have applied a three-parameter function of

$$M_1 + M_2 T^{M_3} \ , \tag{3.22}$$

where T is the ToF and M_i ($i = 1$ to 3) are the fitting parameters. The obtained background shapes are shown in Figure 3.3.

3.2.4 Neutron Transmission Enhancement and its Relation to NMR

As shown in Subsection 3.1.2, the $P_{^3He}\varrho_{^3He}\sigma_{^3He}$ is obtained from the measurements of the transmission enhancements of the polarizer and the analyzer. Using Equation (3.12), the transmission enhancements of the polarizer and the analyzer are respectively as

$$T_E(\hat{P}_{pol}, \varrho_{pol}) = \cosh\left(\hat{P}_{pol}\varrho_{pol}\sigma_{^3He}\right) \tag{3.23}$$

and

$$T_E(\hat{P}_{ana}, \varrho_{ana}) = \cosh\left(\hat{P}_{ana}\varrho_{ana}\sigma_{^3He}\right) \ . \tag{3.24}$$

Here $\hat{P}_{pol}$ and $\hat{P}_{ana}$ denotes the polarization of the polarizer and the analyzer, respectively, when the transmission enhancements were measured.

Since the neutron cross section on ^3He nucleus follows the "$1/v$-rule", the energy dependence of the cross section is given as;

$$\sigma_{^3He}(E_n) = \frac{\sigma_1}{\sqrt{E_n(\mathrm{eV})}} \ , \tag{3.25}$$

where σ_1 is a constant representing $\sigma_{^3He}$ at 1 eV. Thus Equations (3.23) and (3.24) are written as

$$T_E(\hat{P}_{pol}, \varrho_{pol}) = \cosh\left(\frac{\hat{P}_{pol}\varrho_{pol}\sigma_1}{\sqrt{E_n}}\right) \tag{3.26}$$

and

$$T_E(\hat{P}_{ana}, \varrho_{ana}) = \cosh\left(\frac{\hat{P}_{ana}\varrho_{ana}\sigma_1}{\sqrt{E_n}}\right) \ . \tag{3.27}$$

These relations determine the neutron-energy dependence of the transmission enhancement. Before the measurements, the lanthanum target was lifted up from the beam path. To measure the transmission of the polarizer, the real cell was placed on the beam path and the polarization of the analyzer was turned off. To measure the transmission of the analyzer, the dummy cell of the polarizer was placed on the beam path to deliver unpolarized beam to the analyzer. The polarization of the ^3He in the real cell was remained polarized during this measurement, but the real cell was moved out from the beam path.

To calculate the transmission enhancements from the obtained neutron time-spectra, the beam intensity was normalized with the beam monitor signal and the γ-ray background was subtracted from the spectra. The obtained transmission enhancements are shown in Figures 3.4 and 3.5. The data have been fit with Equations (3.26) and (3.27), and we have obtained

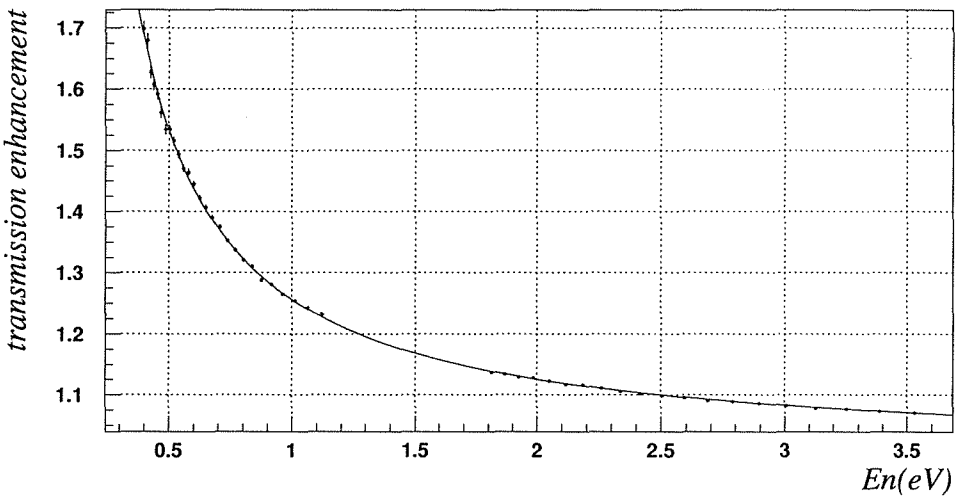

Figure 3.4: Obtained transmission enhancement on the polarizer.

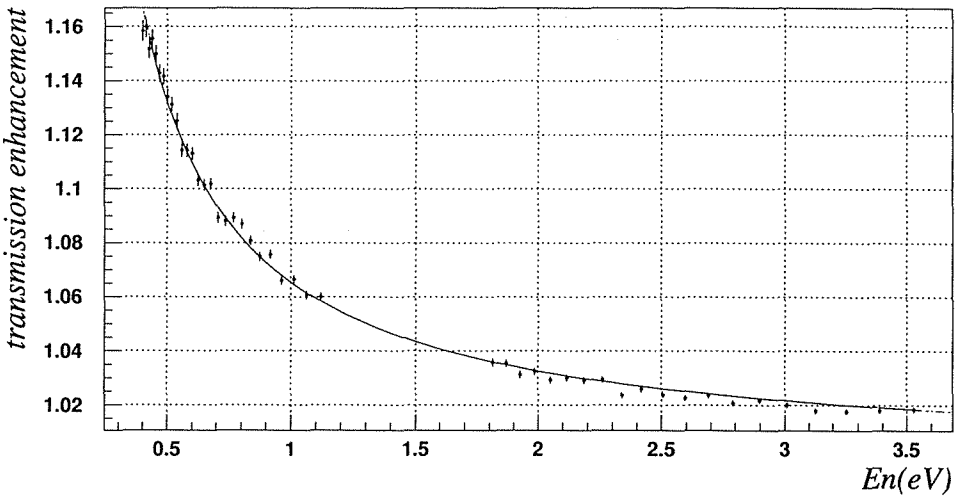

Figure 3.5: Obtained transmission enhancement on the analyzer.

$$\hat{P}_{pol}\varrho_{pol}\sigma_1 = (\,0.7043 \pm 0.0006\,)\ \sqrt{\mathrm{eV}} \tag{3.28}$$

and

$$\hat{P}_{ana}\varrho_{ana}\sigma_1 = (\,0.3613 \pm 0.0007\,)\ \sqrt{\mathrm{eV}}\ . \tag{3.29}$$

Since the thickness of the both spin filters were 6 atm $\times$ 10 cm, the polarizations of the ^3He in the polarizer and the analyzer have been evaluated as $\hat{P}_{pol} = 0.56$, and $\hat{P}_{ana} = 0.29$.

Since the relative polarizations of ^3He in the polarizer and the analyzer were sequentially measured during the experiment by means of AFP-NMR, the NMR signals can be used to trace the change of the polarizations. Thus at given time, t, the polarizations of P_{pol} when the NMR signal is N_{pol} can be obtained as

$$P_{pol} = \frac{N_{pol}}{\hat{N}_{pol}}\hat{P}_{pol}\ , \tag{3.30}$$

where $\hat{N}_{pol}$ denotes the average of the NMR signal taken during the measurement of the transmission enhancement. The same relation also holds for the analyzer,

$$P_{ana} = \frac{N_{ana}}{\hat{N}_{ana}}\hat{P}_{ana}\ . \tag{3.31}$$

3.2.5 Determination of the Shape of the P-wave Resonance of ^{139}La

In order to determine the energy, E_p, and the width, Γ_p, of the 0.74-eV p-wave resonance of ^{139}La, the neutron transmission around the resonance has been analyzed.

The ratio of the neutron transmission with the lanthanum target, T^{La}, to that without the target, T^{empty}, can be written as

$$\frac{T^{La}}{T^{empty}} = A_s \exp\left(-N\sigma_p l\right), \tag{3.32}$$

where N, σ_p, and l are the number density of the ^{139}La nuclei, the p-wave cross section and the length of the target, respectively, and A_s is the neutron attenuation due to all other effects but the p-wave resonance.

A quadratic function of E_n, which has 3 fitting parameters, has been applied as an empirical function for A_s. The $N\sigma_p l$ has been parametrized with 3 fitting parameters as

$$N\sigma_p l = \frac{D}{1 + \left(\frac{E_n - E_p}{\Gamma_p/2}\right)^2}\ , \tag{3.33}$$

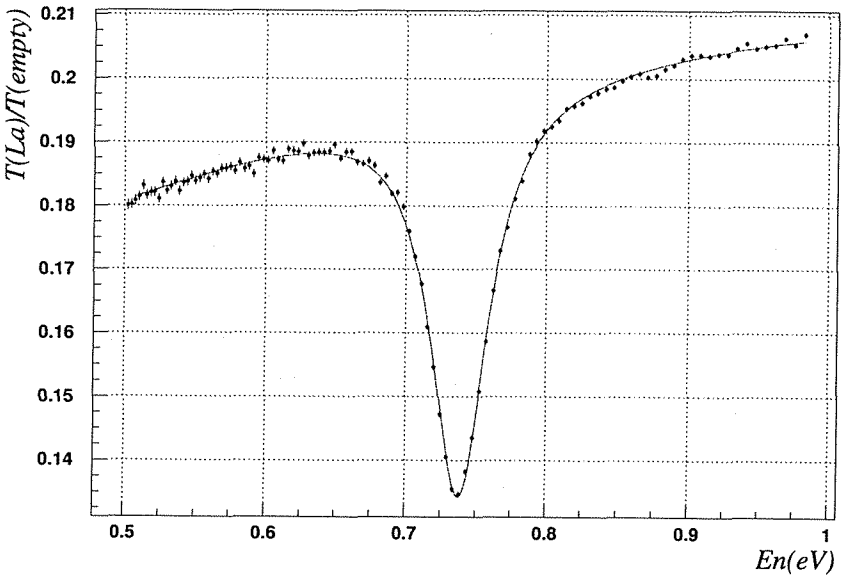

Figure 3.6: The 0.74-eV p-wave resonance of ^{139}La with the fitting curve.

where D, E_p, and Γ_p are the depth, the energy, and the width of the p-wave resonance, respectively, and E_n is the neutron energy determined from ToF.

The count on the transmission detector has been normalized with the flux monitor and subtracted with the γ-ray background. The ratio of the corrected counts with the target to that without the target gives the energy dependence of the Equation (3.32). The result is plotted in Fig. 3.6 together with the determined fitting function.

We have obtained

$$E_p = (0.7379 \pm 0.0009)\,\mathrm{eV}\,, \tag{3.34}$$

$$\Gamma_p = (0.0449 \pm 0.0027)\,\mathrm{eV}\,. \tag{3.35}$$

These values have been used in the analysis of the rotation angle, and in the extraction of the weak matrix element from the rotation angle.

3.2.6 Extraction of Spin Rotation Angle

In order to eliminate the spin rotation caused by the residual magnetic field, we modeled the observed A^{La} to follow the relation as

$$A^{La} = \phi_{pp} \cdot \frac{\frac{E_n - E_p}{\Gamma_p/2}}{1 + \left(\frac{E_n - E_p}{\Gamma_p/2}\right)^2} + C + SA^{empty} \ . \tag{3.36}$$

Here the first term is the signal of the spin rotation angle caused by the parity nonconserving interaction, C represents the error of the angle adjustment between the polarizer and the analyzer, and SA^{empty} is the effect of the residual magnetic field. The ϕ_{pp} is a peak-to-peak value of the dispersion shape of the energy dependence in the spin rotation angle. From Equation (1.1), ϕ_{pp} is described as

$$\phi_{pp} = \frac{8\pi g N l}{k_n^2 \Gamma_p} \frac{xW(\Gamma_s^n \Gamma_p^n)^{\frac{1}{2}}}{E_p - E_s} \ , \tag{3.37}$$

where l is the target length.

Here we assume that the fake rotation pattern in A^{La} is as same as that of A^{empty}. Naively thinking S is equal to unity. The parameter S, however, is introduced to account for any systematics between the empty runs and the runs with the target, which include possible errors in the NMR measurements of the polarizer as described in Subsection 3.2.2 .

The observed rotation angles, A^{La} and A^{empty}, are plotted in Figure 3.7 . By applying Equation (3.36), we have obtained fitting parameters as;

$$\phi_{pp} = (3.99 \pm 0.55) \times 10^{-2} \, \text{rad} \ , \tag{3.38}$$

$$C = (3.79 \pm 0.95) \times 10^{-3} \tag{3.39}$$

and

$$S = 1.115 \pm 0.012 \ . \tag{3.40}$$

In the fitting the chi square, χ^2, has been 81.8 and the degree of freedom, DoF, has been 47. The parameters, E_p and Γ_p, have been fixed with the values obtained from the analysis of the resonance shape described in Subsection 3.2.5. Since the ratio of the chi square to the degree of freedom is significantly larger than unity, the errors of the fitting parameters have been rescaled with a factor of $\sqrt{\chi^2/DoF}$. Accordingly, the parameter error in Equation (3.38) has been modified to

$$\phi_{pp} = (3.99 \pm 0.73) \times 10^{-2} \, \text{rad} \ . \tag{3.41}$$

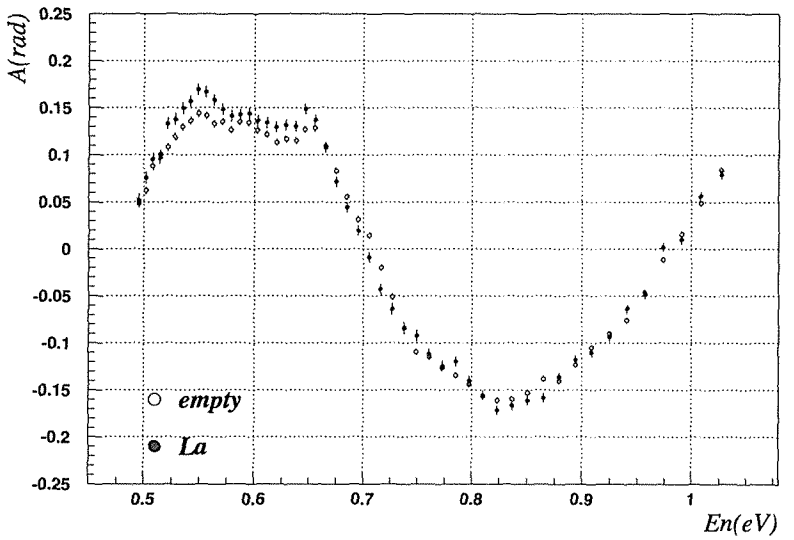

Figure 3.7: Obtained A^{La} and A^{empty}. The closed and open circles represent A^{La} and A^{empty}, respectively.

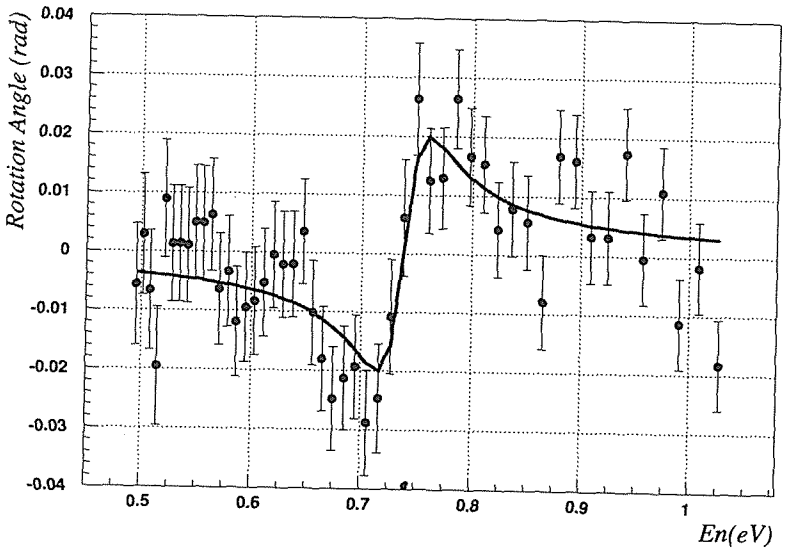

Figure 3.8: The spin rotation angle in the 0.74-eV p-wave resonance of ^{139}La. The solid line represents the obtained energy dependence of the rotation angle.

Figure 3.8 shows the plot of the signal component ($A^{La} - C - SA^{empty}$) with the determined function of the first term in Equation (3.36). The spin rotation signal has been clearly observed.

In order to ensure the validity of the analysis, we have repeated the same procedure for the weak field data, in which the field strength of the spin transport magnets were reduced as described in Section 2.4. The observed rotation angles, A^{La} and A^{empty}, are shown in Figure 3.9, and the extracted spin precession curvature is shown in Figure 3.10 together with the best fit. The fitting parameters have been obtained as;

$$\phi_{pp} = (3.42 \pm 0.76) \times 10^{-2}\,\mathrm{rad}\ , \tag{3.42}$$

$$C = (-3.26 \pm 1.42) \times 10^{-3} \tag{3.43}$$

and

$$S = 1.041 \pm 0.011\ , \tag{3.44}$$

with $\chi^2 = 54.2$ and $DoF = 47$. In this fitting, the ratio of the chi square to the degree of freedom has been obtained close to unity. The obtained amplitudes of the spin rotations have been found to be consistent to each other between the two settings.

Since the target was 5 cm in length, the peak-to-peak rotation angle for the unit length, $\frac{\partial \phi_{pp}}{\partial z}$, has been obtained from the strong field measurement as

$$\frac{\partial \phi_{pp}}{\partial z} = (8.0 \pm 1.5) \times 10^{-3}\,\mathrm{rad/cm}\ , \tag{3.45}$$

and also from the weak field measurement as

$$\frac{\partial \phi_{pp}}{\partial z} = (6.8 \pm 1.5) \times 10^{-3}\,\mathrm{rad/cm}\ . \tag{3.46}$$

The errors of each fit parameter shown above have been determined as a maximal variance of the parameter with keeping the increase of the χ^2 value by unity. The two values of the neutron spin rotation shown in Equations (3.45) and (3.46) obtained in the different magnetic-field settings are consequently consistent to each other. By combining these two results, we have obtained the peak-to-peak amplitude of the spin rotation as

$$\frac{\partial \phi_{pp}}{\partial z} = (7.44 \pm 1.05) \times 10^{-3}\,\mathrm{rad/cm}\ . \tag{3.47}$$

It should be mentioned that the present analysis procedure absorbs the systematics in the polarization measurements. The ambiguity in the polarization measurements by means of the transmission enhancement are negligible compared to the

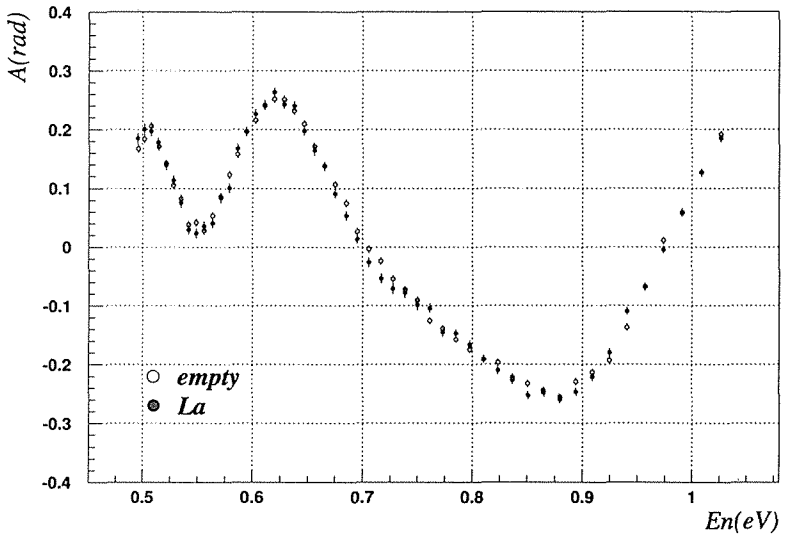

Figure 3.9: Obtained A^{La} and A^{empty} from the weak field data. The closed and open circles represent A^{La} and A^{empty}, respectively.

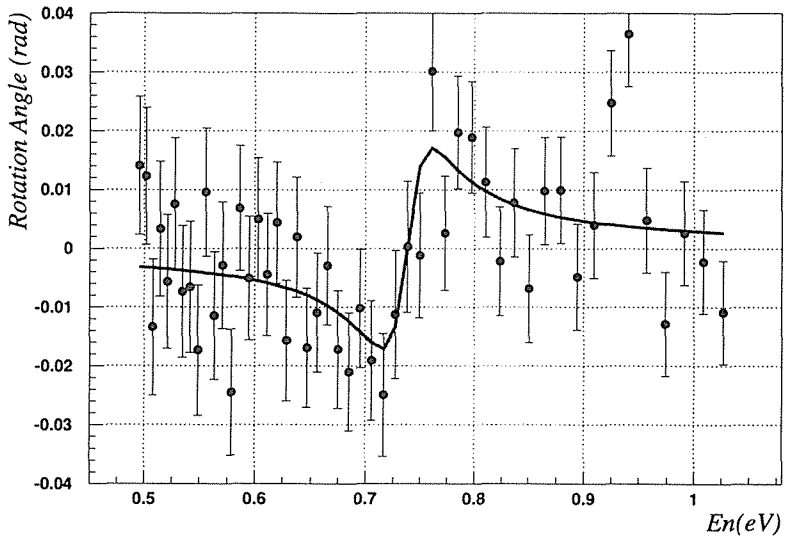

Figure 3.10: Obtained rotation angle from the weak field data. The solid line represents the obtained energy dependence of the rotation angle.

error of the fitting parameters. The ambiguity of the absolute polarization remains only from the sensitivity change due to the gimbal mount rotation. Thus as the final value we have obtained

$$\frac{\partial \phi_{pp}}{\partial z} = (7.44 \pm 1.09) \times 10^{-3}\,\mathrm{rad/cm}\ . \tag{3.48}$$

Here we include the ambiguity of absolute scale added to the statistically determined error.

Chapter 4

Results and Discussion

The parity nonconserving spin rotation angle of neutrons transmitted through a ^{139}La target in the 0.74-eV p-wave resonance has been measured. The peak-to-peak value of the rotation angle for the target of 1-cm long has been obtained as

$$\frac{\partial \phi_{pp}}{\partial z} = (7.44 \pm 1.09) \times 10^{-3}\ \mathrm{rad/cm}\ . \tag{4.1}$$

In Table 4.1, all the data on $\frac{\partial \phi_{pp}}{\partial z}$ presently available are shown. For the result of the ILL experiment [23] using cold neutrons, the peak-to-peak value has been estimated by us, assuming that the energy dependence of the rotation angle follows Equation (1.1). Although our experimental method is similar to that of the KEK experiment[20], our result is closer to the estimation from the result of the ILL experiment. The three experimental results including the present work are consistent to each other within the errors. Our experimental errors for the neutron spin rotation angle is smaller than those obtained in KEK.

The method applied in the present work has the energy resolution of 10 meV, which is substantially smaller than the width of the p-wave resonance, 45 meV. From the viewpoint to determine the absolute amplitude of the spin rotation, our

$\frac{\partial \phi_{pp}}{\partial z}(10^{-3}\mathrm{rad/cm})$	energy region	facility	reference
7.13 ± 0.94	cold	ILL	[23]
4.62 ± 1.72	in resonance	KEK	[20]
7.44 ± 1.09	in resonance	LANSCE	present work

Table 4.1: List of the peak-to-peak values in the neutron spin rotation in the 0.74-eV p-wave resonance of ^{139}La.

xW(meV)	observed quantity	energy region	facility	reference
1.7 ± 0.1	longitudinal asymmetry	in resonance	KEK	[11]
1.68 ± 0.06	longitudinal asymmetry	in resonance	LANSCE	[32]
1.77 ± 0.13	longitudinal asymmetry	in resonance	Gatchina	[22]
1.28 ± 0.12	longitudinal asymmetry	in resonance	Dubna	[33]
1.27 ± 0.20	longitudinal asymmetry	thermal	LINP	[8]
1.63 ± 0.21	spin rotation angle	cold	ILL	[23]
1.00 ± 0.37	spin rotation angle	in resonance	KEK	[20]
1.71 ± 0.25	spin rotation angle	in resonance	LANSCE	present work

Table 4.2: List of values of xW of the 0.74-eV p-wave resonance of ^{139}La.

method has an advantage over the experiments using the crystal-diffraction method [22, 24].

We assume that the spin rotation angle in the p-wave resonance is caused only by the interference with the s-wave resonance at neutron energies of -48.6 eV. Using Equation (1.1), we have obtained the value of xW from the experimental data of $\frac{\partial \phi_{pp}}{\partial z}$ as

$$xW = (1.71 \pm 0.25)\ \text{meV} . \tag{4.2}$$

In the extraction of xW from the rotation angle, E_p and Γ_p have been determined with the present data by fitting the p-wave resonance, and the values of g, E_s, Γ_p^n, and Γ_s^n in the reference [31] have been used. The experimental results of xW which were obtained previously besides our data are listed in Table 4.2. These values are plotted in Figure 4.1. The closed circles are the values from the longitudinal asymmetries measured in the resonance [11, 32, 22, 33]. The closed triangle is of the longitudinal asymmetry measured in the low energy tail [8]. The open triangle is of the spin rotation angle measured in the low energy tail [23]. The open circles are of the spin rotation angles measured in the resonance [20]. If we average all the results in the table, we can obtain

$$xW = (1.62 \pm 0.04)\ \text{meV} . \tag{4.3}$$

The average is also shown in Figure 4.1.

The obtained value of xW in this experiment is consistent with those obtained from the longitudinal asymmetries within one standard deviation. It should be noted that the measurement of the spin rotation angle is independent of the measurement of the longitudinal asymmetry. It is meaningful that the parity nonconserving matrix element, xW, has been obtained consistently from the independent measurements.

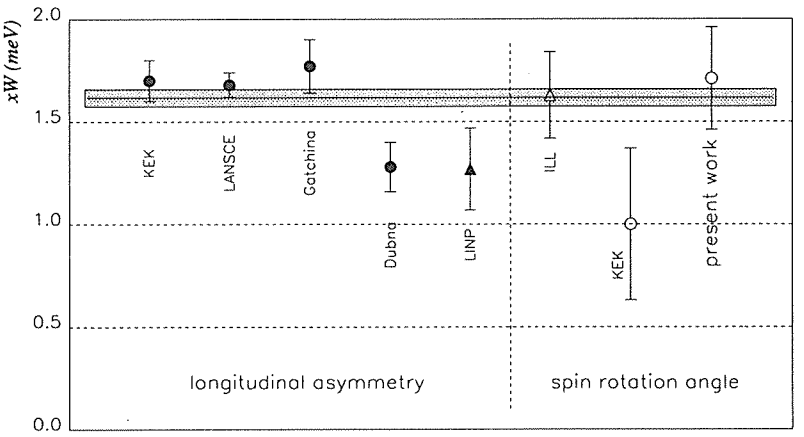

Figure 4.1: The experimental values of the mixing matrix element xW. The closed circles are the values from the longitudinal asymmetries measured in the resonance [11, 32, 22, 33]. The closed triangle is of the longitudinal asymmetry measured in the low energy tail [8]. The open triangle is of the spin rotation angle measured in the low energy tail [23]. The open circles are of the spin rotation angles measured in the resonance [20]. The average of all the data is shown as the band.

The consistency between the real and the imaginary parts of F_3, which is the parity nonconserving amplitude introduced in Section 1.2, has been confirmed with this work.

One can see in Figure 4.1 that the values of xW obtained in the resonance and those in the low energy tail of the p-wave resonance are consistent with each other. The longitudinal asymmetry and the rotation angle in the tail are less than $\frac{1}{30}$ and $\frac{1}{900}$, respectively, compared to those in the resonance. This implies that the s-p mixing picture is valid to account for the enhancement of parity violation in neutron induced nuclear reaction on ^{139}La.

From the viewpoint of the experimental technique, this experiment has established the flippable polarized ^3He neutron-spin filter. In our experiment flipping of the polarization direction of ^3He has been carried out for the spin filter in front of the target in the neutron beam. Such an equipment is regarded to be applied to the polarizer and the analyzer for the test of time reversal invariance in future, since time reversal invariance can be tested with low energy neutrons propagating through polarized target materials according to Stodolsky [34]. Flipping the directions of the polarizations of the spin filters located upstream and downstream of the target is

required in the test of violation of time reversal invariance. The technique achieved in our experiment is applicable to the test of time reversal invariance.

Chapter 5

Conclusion

We have measured the parity nonconserving spin rotation of neutrons transmitted through a ^{139}La target in the 0.74-eV p-wave resonance at MLNSC in LANSCE.

Two sets of the polarized ^3He filters have been used. One of them has been used for polarizing the neutron beam and the other for analyzing the polarization of the neutron after passing through the 5cm-thick lanthanum target. The two spin filters have been polarized transversely to the beam direction and perpendicular to each other in order to measure the neutron spin rotation around the beam direction. The rotation angle has been deduced from the asymmetry of the neutron transmission by flipping the polarization direction of the neutron spin polarizer by means of AFP-NMR. The neutron spin rotation has been obtained as

$$\frac{\partial \phi_{pp}}{\partial z} = (7.44 \pm 1.09) \times 10^{-3}\,\mathrm{rad/cm}\ . \tag{5.1}$$

The result is consistent with the previous measurements within the errors but the accuracy of the value of the spin rotation has been greatly improved.

From the viewpoint of the s-p mixing model, the parity nonconserving neutron spin rotation is caused by the interference between the p-wave resonance and its neighboring s-wave resonance. Considering that the s-wave resonance at -48.6 eV interferes with the 0.74-eV p-wave resonance, we have obtained the weak mixing matrix element with the $j = 1/2$ component as

$$xW = (1.71 \pm 0.25)\,\mathrm{meV}\ . \tag{5.2}$$

The value agrees well with the results previously obtained by the measurements of the longitudinal asymmetry for the cross section in the same resonance within the errors.

The present work has confirmed that the large enhancement of parity nonconserving effect exists in the neutron spin rotation. It has been found that the enhancements in the longitudinal asymmetry and the spin rotation can consistently be described by the s-p mixing model.

Acknowledgements

To accomplish this work, the author is indebted to many people of his colleagues. The author would like to express his thankfulness to them.

First of all, he wishes to express his sincere thanks to Prof. A. Masaike who gave a chance to the author to be engaged in the study of fundamental physics with low energy neutrons. If it had not been for his continuous support and advice, the author could not have made this work completed.

The author expresses his special gratitude to Prof. K. Asahi who is a spokesperson of the collaboration of the present experiment. The experiment was carried out owing to the efforts of Prof. K. Asahi, Dr. J.D. Bowman, Dr. P.P.J. Delheij, Dr. H. Funahashi, Prof. S. Ishimoto, Dr. G. Jones, Prof. A. Masaike, Prof. Y. Masuda, Dr. Y. Matsuda, Prof. K. Morimoto, Dr. S. Muto, Dr. S.I. Penttilä, Dr. V.R. Pomeroy, Dr. K. Sakai, Dr. E.I. Sharapov, Dr. D.A. Smith, and Dr. V.W. Yuan. As well as the execution of the experiment, discussions with the members were quite valuable for the author.

Prof. H. En'yo has been giving the author advice on the analysis of this work. Prof. K. Imai has encouraged the author to complete this work.

This work has been partially supported by Fellowships of the Japan Society for the Promotion of Science for Japanese Junior Scientists.

Appendix A

Optical Pumping

In the present experiment, the ^3He nuclei were polarized by optical pumping method using rubidium atoms. In this method, an exposure of circularly polarized photons, the energy of which is the same as the level spacing of the atoms, promotes transitions from the lower to the higher level. In the experiment, we used the transition of rubidium atoms from the ground state $5^2S_{\frac{1}{2}}$ to the excited state of 1.56 eV $5^2P_{\frac{1}{2}}$ with the photons produced by laser diode arrays. The laser light was transmitted through a quarter wave plate to be circularly polarized.

When circularly polarized light, $\sigma_+(m = +1)$, of 1.56 eV is exposed to a rubidium atom, because of the conservation of angular momentum, only the light-absorbing transition from $5^2S_{\frac{1}{2}}(m = -\frac{1}{2})$ to $5^2P_{\frac{1}{2}}(m = +\frac{1}{2})$ is allowed. The excited states

$5^2P_{\frac{1}{2}}(m = +\frac{1}{2})$ emits a photon of almost the same energy, and falls to either of the ground states $5^2S_{\frac{1}{2}}(m = \pm\frac{1}{2})$. The branching ratios are, which are determined with Clebsch-Gordan coefficients, $\frac{2}{3}$ for the transition to $5^2S_{\frac{1}{2}}(m = -\frac{1}{2})$, and $\frac{1}{3}$ to $5^2S_{\frac{1}{2}}(m = +\frac{1}{2})$.

Since photons emitted from the excited state $5^2P_{\frac{1}{2}}(m = +\frac{1}{2})$ are not completely polarized, those photons are reabsorbed by rubidium atoms, and limit the polarization of rubidium. The effect is called radiation trapping. In order to avoid this phenomenon, a small amount of nitrogen gas was mixed so that nitrogen molecules and rubidium atoms collide with each other. The rubidium atoms in the excited state $5^2P_{\frac{1}{2}}(m = \pm\frac{1}{2})$ give their excitation energy to rotation or oscillation energy of the nitrogen molecules and then fall into the ground state $5^2S_{\frac{1}{2}}(m = \pm\frac{1}{2})$. Since the rubidium atoms can make a transition into the ground state without emitting any photon in these processes, the radiation trapping doesn't occur. At the same time, the excited states $5^2P_{\frac{1}{2}}(m = \pm\frac{1}{2})$ mix into each other (collisional mixing). With a mixture of nitrogen gas about 100 Torr at room temperature, rubidium atoms of the ground state $5^2S_{\frac{1}{2}}(m = -\frac{1}{2})$, after the absorbing circular polarized photon, make a transition via an excited state $5^2P_{\frac{1}{2}}(m = +\frac{1}{2})$ into the ground states $5^2S_{\frac{1}{2}}(m = \pm\frac{1}{2})$ with almost equal probabilities. Thus rubidium atom is still polarized by illuminating the circularly polarized light.

Spin exchange between rubidium atom and ^3He nucleus, which happens in the collision between ^3He gas and vapor of rubidium atom, raises the nuclear polarization of the ^3He.

Appendix B

Principle of Adiabatic Fast Passage NMR

In the present experiment, a method of AFP-NMR (Adiabatic Fast Passage Nuclear Magnetic Resonance) was used to measure the relative ^3He polarizations of the polarizer and the analyzer. The method was also used in order to flip the ^3He polarization of the polarizer.

Since the magnetic moment $\boldsymbol{\mu}$ and the spin $\boldsymbol{S}$ of the ^3He nucleus is parallel to each other,

$$\boldsymbol{\mu} = \boldsymbol{S}\,\frac{\mu}{s\hbar}\,, \tag{B.1}$$

where μ and s are the size of the magnetic moment and the spin, respectively. The values are $\mu = -2.128\mu_N$ and $s = 1/2$, where μ_N is the nuclear magneton. The motion of the magnetic moment is described as;

$$\frac{d}{dt}\boldsymbol{\mu} = -\gamma\,\boldsymbol{B}\times\boldsymbol{\mu}\ , \tag{B.2}$$

where $\gamma = \frac{\mu}{s\hbar}$. This is so-called Larmor precession whose an angular velocity is $-\gamma\boldsymbol{B}$. Seeing it from the rotating frame whose angular velocity is $\boldsymbol{\omega}$, the movement of the magnetic moment obeys to

$$\frac{d'}{dt}\boldsymbol{\mu} = (-\gamma\,\boldsymbol{B} - \boldsymbol{\omega})\times\boldsymbol{\mu}\ , \tag{B.3}$$

where $\frac{d'}{dt}$ denotes the time derivative in the rotating system. Thus the movement of the magnetic moment in the magnetic field $\boldsymbol{B}$ in the rotating system is the same as that in an effective field,

$$\boldsymbol{B}_{eff} = \boldsymbol{B} + \frac{\boldsymbol{\omega}}{\gamma}\,. \tag{B.4}$$

When AFP-NMR is used, a spin holding field, $\boldsymbol{B}_0$, is applied as a main component of the magnetic field, and also an RF oscillating field $2\boldsymbol{B}_1\cos(\omega t)$ is applied perpendicular to $\boldsymbol{B}_0$. Since the RF oscillating field can be regarded as a sum of two rotating fields whose angular velocities are $\pm\boldsymbol{\omega}$, $\boldsymbol{\omega}$ can be taken parallel to $\boldsymbol{B}_0$. Viewing the system on the rotating frame, one is seen to be at rest and the other is seen to be rotating with $-2\boldsymbol{\omega}$. In the case that the Larmor precession caused by the spin holding field is close to $\boldsymbol{\omega}$ namely

$$-\gamma\boldsymbol{B}_0 \simeq \boldsymbol{\omega}\ , \tag{B.5}$$

the magnetic moment is almost at rest in the rotating system. Thus one of the component of the RF oscillating field keeps the angle to the magnetic moment. And the other is seen to be rotating at $-2\boldsymbol{\omega}$ in angular velocity. Accordingly the effect to the magnetic moment from the rotating component becomes negligible. A a result an effective field in the rotating system is regarded as;

$$\boldsymbol{B}_{eff} = \boldsymbol{B}_0 + \frac{\boldsymbol{\omega}}{\gamma} + \boldsymbol{B}_1'\,, \tag{B.6}$$

where $\boldsymbol{B}_1'$ is a static magnetic field in the rotating system and its strength is B_1. Since the direction of $\boldsymbol{B}_1'$ is perpendicular to $\boldsymbol{B}_0$ and $\frac{\boldsymbol{\omega}}{\gamma}$, the direction of the effective field makes an angle θ_{eff} to the holding field as

$$\tan\theta_{eff} = \frac{B_1}{B_0 + \frac{\omega}{\gamma}} \ . \tag{B.7}$$

When the strength of the spin holding field B_0 is varied, θ_{eff} is changed. If the change of the θ_{eff} is slow enough, the magnetic moment follows the direction of the effective field. Thus the direction of the magnetic moment makes an angle θ_μ to the holding field as;

$$\tan\theta_\mu = \pm\frac{B_1}{B_0 + \frac{\omega}{\gamma}} \ , \tag{B.8}$$

where the sign denotes whether the magnetic moment is parallel or antiparallel to the effective field. Considering the situation that the varying of B_0 changes the sign of $B_0 + \frac{\omega}{\gamma}$ and that the variation is much larger than B_1, the direction of the magnetic moment is inclined and finally flipped. Viewing from the laboratory frame, the magnetic moment is inclined and finally flipped with rotating with an angular velocity of ω . If the RF oscillating field is shut down after the flipping of the polarization and then the strength of the holding field is put back, the magnetic moment remains flipped. We used this technique for the flipping of the ^3He polarization in the polarizer.

With putting a pick-up coil to detect the rotation of the magnetic moment, NMR signal can be read out as an induced voltage. Since the magnetic moment is rotating synchronously to the RF oscillating field, the induced voltage is also oscillating at the same frequency. We used a lock-in amplifier to make a phase-lock analysis of the induced voltage.

Bibliography

[1] C.S. Wu et al., Phys. Rev. 105,1413(1957)

[2] D.E. Nagle et al., in High Energy Physics with Polarized Beams and Targets, ed. G.H. Thomas, AIP Conferetnce Proceedings No.51, (American Institute of Physics, New York, 1978) p.224

[3] R. Balzer et al., Phys. Rev. C30,1409(1984)

[4] P.von Rossen et al.,Polarization Phenomena in Nuclear Physics-1980, Santa Fe, des. D.E. Nagle et al., AIP Conference Proceedeings No.69, (American Institute of Physics, New York, 1981) p.1442

[5] A.R. Bordoz et al., Nucl. Phys. A629,433(1998)

[6] V. Yuan et al., Phys. Rev. Lett 57, 1680(1986)

[7] M. Forte et al., Phys.Rev.Lett. 45,2088(1980)

[8] E.A. Kolomensky et al., Phys. Lett. 107B,272(1981)

[9] V.P. Alfimenkov et al., JETP Lett. 34,295(1981)

[10] Y. Masuda et al., Nucl.Phys. A478,737(1988)

[11] H.M. Shimizu et al., Nucl.Phys. A552,293(1993)

[12] X. Zhu et al., Phys. Rev. C46,768(1992)

[13] C. Francle et al., Phys. Rev. C46,779(1992)

[14] J. Szymanski et al., Phys. Rev. C53,2576(1996)

[15] E.I. Sharapov, Phys. Rev. C59,1772(1999)

[16] S. Stephenson, Ph.D. thesis, North Carolina State University (1996)

[17] L.Y. Lowie, Ph.D. thesis, North Carolina State University (1996)

[18] B.E. Crawford, Ph.D. thesis, Duke University (1997)

[19] Y. Matsuda, Ph.D. thesis, Kyoto University (1998)

[20] K. Sakai, Ph.D. thesis, Tohoku University (1994)

[21] K. Sakai et al., Phys.Let. B391,11(1997)

[22] A.P. Serebrov et al., JETP Lett. 62,545(1995)

[23] B. Heckel et al., Phys.Rev.C29 , 2389(1984)

[24] A. Petoukhov, private communications. Preliminary result was presented at the 6th International Seminar on Interaction of Neutrons with Nuclei, Dubna, Russia.

[25] P.W. Lisowski et al. Nucl.Sci. and Eng. 106,208(1990)

[26] N. Roberson et al., Nucl. Inst. and Methods in Phys. Research A326,549(1993)

[27] J. Szymanski et al., Nucl. Inst. and Methods in Phys. Research A340,564(1994)

[28] L. Passell et al., Phys. Rev. 150, 146(1966)

[29] J. Als-Nielsen and O. Dietrich, Phys. Rev. 133, B925(1964)

[30] Y.-F. Yen et al., in Time Reversal Invariance and Parity Violation in Neutronn Reactions, (World Scientific, Singapore, 1994) 210(1994)

[31] S.F. Mughabghab et al., Neutron Cross Sections, vol. 1A and 1B, (Academic Press, New York) (1988)

[32] V.W. Yuan et al., Phys.Rev. C44,2187(1991)

[33] V.P. Alfimenkov et al., Nucl. Phys. A398, 93(1983)

[34] L. Stodolsky, Phys,Lett. B172,5(1986)